The Astrophysical Journal, 974:147 (16pp), 2024 October 10 https://doi.org/10.3847/1538-4357/ad6565

A SPectroscopic Survey of Biased Halos In the Reionization Era (ASPIRE): Broad-line AGN at $z = 4-5$ Revealed by JWST/NIRCam WFSS

Xiaojing Lin[1,2], Feige Wang[2], Xiaohui Fan[2], Zheng Cai[1], Jaclyn B. Champagne[2], Fengwu Sun[2,3], Marta Volonteri[4], Jinyi Yang[2], Joseph F. Hennawi[5,6], Eduardo Bañados[7], Aaron Barth[8], Anna-Christina Eilers[9], Emanuele Paolo Farina[10], Weizhe Liu[2], Xiangyu Jin[2], Hyunsung D. Jun[11], Alessandro Lupi[12,13,14], Koki Kakiichi[15,16], Chiara Mazzucchelli[17], Masafusa Onoue[18,19,20], Zhiwei Pan[20,21], Elia Pizzati[6], Sofía Rojas-Ruiz[22], Jan-Torge Schindler[23], Benny Trakhtenbrot[24], Yue Shen[25,26], Maxime Trebitsch[27], Ming-Yang Zhuang[25], Ryan Endsley[28], Romain A. Meyer[7], Zihao Li[1], Mingyu Li[1], Maria Pudoka[2], Wei Leong Tee[2], Yunjing Wu[1], and Haowen Zhang[2]

[1] Department of Astronomy, Tsinghua University, Beijing 100084, People's Republic of China; linxj21@mails.tsinghua.edu.cn
[2] Steward Observatory, University of Arizona, 933 N. Cherry Ave., Tucson, AZ 85721, USA
[3] Center for Astrophysics | Harvard & Smithsonian, 60 Garden St., Cambridge, MA 02138, USA
[4] Institut d'Astrophysique de Paris, Sorbonne Université, CNRS, UMR 7095, 98 bis bd Arago, 75014 Paris, France
[5] Department of Physics, Broida Hall, University of California, Santa Barbara, Santa Barbara, CA 93106-9530, USA
[6] Leiden Observatory, Leiden University, P.O. Box 9513, NL-2300 RA Leiden, The Netherlands
[7] Max Planck Institut für Astronomie, Königstuhl 17, D-69117, Heidelberg, Germany
[8] Department of Physics and Astronomy, 4129 Frederick Reines Hall, University of California, Irvine, CA 92697-4575, USA
[9] MIT Kavli Institute for Astrophysics and Space Research, Massachusetts Institute of Technology, Cambridge, MA 02139, USA
[10] Gemini Observatory, NSF's NOIRLab, 670 North A'ohoku Place, Hilo, HI 96720, USA
[11] Department of Physics, Northwestern College, 101 7th St. SW, Orange City, IA 51041, USA
[12] Dipartimento di Scienza e Alta Tecnologia, Università degli Studi dell'Insubria, via Valleggio 11, I-22100, Como, Italy
[13] INFN, Sezione di Milano-Bicocca, Piazza della Scienza 3, I-20126 Milano, Italy
[14] Dipartimento di Fisica "G. Occhialini," Università degli Studi di Milano-Bicocca, Piazza della Scienza 3, I-20126 Milano, Italy
[15] Cosmic Dawn Center (DAWN), Denmark
[16] Niels Bohr Institute, University of Copenhagen, Jagtvej 128, 2200 Copenhagen N, Denmark
[17] Instituto de Estudios Astrofísicos, Facultad de Ingeniería y Ciencias, Universidad Diego Portales, Avenida Ejercito Libertador 441, Santiago, Chile
[18] Kavli Institute for the Physics and Mathematics of the Universe (Kavli IPMU, WPI), The University of Tokyo Institutes for Advanced Study, The University of Tokyo, Kashiwa, Chiba 277-8583, Japan
[19] Center for Data-Driven Discovery, Kavli IPMU (WPI), UTIAS, The University of Tokyo, Kashiwa, Chiba 277-8583, Japan
[20] Kavli Institute for Astronomy and Astrophysics, Peking University, Beijing 100871, People's Republic of China
[21] Department of Astronomy, School of Physics, Peking University, Beijing 100871, People's Republic of China
[22] Department of Physics and Astronomy, University of California, Los Angeles, 430 Portola Plaza, Los Angeles, CA 90095, USA
[23] Hamburger Sternwarte, Universität Hamburg, Gojenbergsweg 112, D-21029 Hamburg, Germany
[24] School of Physics and Astronomy, Tel Aviv University, Tel Aviv 69978, Israel
[25] Department of Astronomy, University of Illinois at Urbana-Champaign, Urbana, IL 61801, USA
[26] National Center for Supercomputing Applications, University of Illinois at Urbana-Champaign, Urbana, IL 61801, USA
[27] Kapteyn Astronomical Institute, University of Groningen, 9700 AV Groningen, The Netherlands
[28] Department of Astronomy, University of Texas, Austin, TX 78712, USA
Received 2024 May 22; revised 2024 July 9; accepted 2024 July 17; published 2024 October 9

Abstract

Low-luminosity active galactic nuclei (AGNs) with low-mass black holes (BHs) in the early universe are fundamental to understanding the BH growth and their coevolution with the host galaxies. Utilizing JWST NIRCam Wide Field Slitless Spectroscopy, we perform a systematic search for broad-line Hα emitters (BHAEs) at $z \approx 4$–5 in 25 fields of the A SPectroscopic survey of biased halos In the Reionization Era (ASPIRE) project, covering a total area of 275 arcmin^2. We identify 16 BHAEs with FWHM of the broad components spanning from $\sim$1000 to 3000 km s^{-1}. Assuming that the broad line widths arise as a result of Doppler broadening around BHs, the implied BH masses range from 10^7 to $10^8 M_\odot$, with broad Hα-converted bolometric luminosities of $10^{44.5}$–$10^{45.5}$ erg s^{-1} and Eddington ratios of 0.07–0.47. The spatially extended structure of the F200W stacked image may trace the stellar light from the host galaxies. The Hα luminosity function indicates an increasing AGN fraction toward the higher Hα luminosities. We find possible evidence for clustering of BHAEs: two sources are at the same redshift with a projected separation of 519 kpc; one BHAE appears as a composite system residing in an overdense region with three close companion Hα emitters. Three BHAEs exhibit blueshifted absorption troughs indicative of the presence of high column density gas. We find that the broad-line-selected and photometrically selected BHAE samples exhibit different distributions in the optical continuum slopes, which can be attributed to their different selection methods. The ASPIRE broad-line Hα sample provides a good database for future studies of faint AGN populations at high redshift.

Unified Astronomy Thesaurus concepts: High-redshift galaxies (734); Active galactic nuclei (16)

1. Introduction

Tremendous efforts have been made in the past decades to search for and characterize supermassive black holes (SMBHs) in distant bright quasars and active galactic nuclei (AGNs; Fan et al. 2023). Luminous quasars at $z > 5$ and black holes (BHs) with masses of $\sim 10^9\ M_\odot$ pose challenges to BH formation theories, with rapid mass assembly within a short amount of cosmic time (e.g., Bañados et al. 2018; Wang et al. 2021; Yang et al. 2021). Such a rapid growth with sustained episodes would erase the imprints of initial BH seeds (Volonteri 2010), necessitating studies of high-redshift, low-mass BHs and low-luminosity AGNs. However, the knowledge of early low-mass BHs was very limited before the launch of James Webb Space Telescope (JWST). With the unprecedented infrared capabilities of JWST, we are now able to observe low-mass, low-luminosity systems, closer to the early stage of BH growth and the predicted seed BH population (Inayoshi et al. 2022). Faint AGNs at high redshift with smaller BHs provide crucial constraints to the BH seeding, growth, and coevolution with galaxies (Ding et al. 2023; Pacucci et al. 2023; Volonteri et al. 2023; Li et al. 2024).

In pursuit of the low-luminosity AGNs (e.g., Übler et al. 2023; Furtak et al. 2024; Kocevski et al. 2023; Onoue et al. 2023), JWST reveals an abundant population of red compact sources at $z > 4$ (e.g., Barro et al. 2023; Labbe et al. 2023), nicknamed "little red dots" (LRDs; Matthee et al. 2023). Their number density is 10–100 × higher than the extrapolation from quasar luminosity functions (LFs; e.g., Kocevski et al. 2023). The nature of LRDs remains a mystery. JWST spectroscopy detects moderately luminous and broad Hα or Hβ lines in the LRDs, suggesting SMBHs with masses ranging from $\sim 10^6$ to $\lesssim 10^9\ M_\odot$ (Furtak et al. 2024; Harikane et al. 2023; Kocevski et al. 2023; Kokorev et al. 2023; Maiolino et al. 2023; Matthee et al. 2023; Greene et al. 2024). Most of them have SMBH masses 1–2 dex lower than those of UV-bright quasars at similar redshifts identified before the launch of JWST (Onoue et al. 2019; Yang et al. 2023). LRDs typically exhibit V-shape spectral energy distributions (SEDs; Furtak et al. 2024; Killi et al. 2023; Labbe et al. 2023; Greene et al. 2024), with the optical continuum redder than that in the UV in the f_λ space (typically the UV continuum slope $\beta_{\rm UV} < 0$ and the optical continuum slope $\beta_{\rm opt} > 1$). Whether the UV emission of LRDs originates from host galaxies or the scattered light of AGNs is still under debate (Kocevski et al. 2023; Labbe et al. 2023; Pérez-González et al. 2024).

However, before a full understanding of the physical nature of LRDs, one of the main areas of uncertainty is the selection criteria. Spectroscopic selections (Harikane et al. 2023; Kocevski et al. 2023; Maiolino et al. 2023; Matthee et al. 2023) are based on the broad Hα or Hβ emission lines, indicative of broad-line regions (BLRs) around BHs. On the other hand, photometric selections are usually based on LRDs' V-shape SED and their compactness and redness (Labbe et al. 2023; Greene et al. 2024; Kokorev et al. 2024; Pérez-González et al. 2024). Some photometrically selected LRD candidates have been confirmed as brown dwarfs spectroscopically (Hainline et al. 2024; Greene et al. 2024). Without showing broadened Balmer emission lines or other AGN line diagnostics (Scholtz et al. 2023), we also cannot rule out the possibility of dusty starburst galaxies. JWST/MIRI studies on photometrically selected LRDs show flattened spectral shape in the rest-frame near-infrared ($\gtrsim 1\ \mu$m), inconsistent with emission from AGN dust tori (Williams et al. 2024; Pérez-González et al. 2024). Pérez-González et al. (2024) claimed that these photometrically selected LRDs are more likely to be extremely intense dusty starburst galaxies with obscured AGNs contributing in the mid-infrared. It is unclear whether the photometrically selected LRDs and the broad-line-selected ones through Wide Field Slitless Spectroscopy (WFSS) or NIRSpec share the same physical properties. Furthermore, it also deserves further exploration to determine whether these LRDs are indeed AGNs.

To better constrain the nature of low-luminosity AGNs, including the so-called LRDs, and study BH mass assembly at high redshifts, we need a large sample of broad-line-selected faint AGNs. In this work, we perform a systemic search for broad Hα line emitters (BHAEs) in the A SPectroscopic survey of biased halos In the Reionization Era (ASPIRE) program (Wang et al. 2023; Yang et al. 2023). ASPIRE is the JWST Cycle 1 grism program covering a large sky area, totaling $\approx$65 hr over $\approx$275 arcmin^2, over 25 different fields. Using JWST/NIRCam WFSS (Greene et al. 2016) in F356W ($R \approx 1600$), we can build up a flux-limited BHAE sample at $z = 4$–5. ASPIRE's large survey area over multiple fields allows us to quantify the number density and AGN fraction, effectively mitigating the cosmic variance. To avoid confusion, we refer to our broad-line-selected sample as BHAEs, rather than LRDs.

This paper is organized as follows. We describe the JWST observations, data reduction, and sample selection in Section 2. In Section 3, we present the properties of our selected BHAE sample, including their spectral properties (Section 3.1), BH masses and bolometric luminosities (Section 3.2), UV and optical continuum slopes (Section 3.3), and morphology (Section 3.4). We analyze the Hα LF in Section 3.5. We discuss interesting individual sources in our sample in Section 4. Our results are summarized in Section 5. Throughout this work, a flat ΛCDM cosmology is assumed, with $H_0 = 70$ km s^{-1} Mpc^{-1}, $\Omega_{\Lambda,0} = 0.7$, and $\Omega_{m,0} = 0.3$. Distances are provided in the comoving frame if not specified.

2. Data and Sample

2.1. JWST Observations

The ASPIRE program (GO 2078; PI F. Wang) targets 25 quasars at $6.5 < z < 6.8$ with JWST/NIRCam imaging and WFSS data, with a total survey area of $\sim 11 \times 25$ arcmin^2. For each field, ASPIRE obtains 2834.5 s exposures in NIRCam/F356W Grism R, accompanied with direct imaging of 1417.3 s in NIRCam/F115W and F356W and 2800 s in F200W. The data are reduced in the same way as described in Wang et al. (2023). We summarize the main procedure below.

The NIRCam images are reduced with the standard pipeline v1.10.2.[29] We utilize the reference files (`jwst_1080.pmap`) from version 11.16.21 of the standard Calibration Reference Data System[30] (CRDS) for calibration. The $1/f$ noise is subtracted on a row-by-row basis and column-by-column basis after `CALWEBB` Stage 1. After Stage 2, a master median background is generated using all available exposures from ASPIRE for each band. The master backgrounds are then scaled and subtracted for individual exposures. All the images

[29] https://github.com/spacetelescope/jwst

[30] https://jwst-crds.stsci.edu

are mosaicked with a pixel scale of 0.″031 and `pixfrac=0.8`. Their World Coordinate System (WCS) is registered using the Gaia Data Release 2 catalog (Gaia Collaboration et al. 2016, 2018). We construct the photometric catalogs with SExtractor++ (Bertin et al. 2020), using F356W as the detection images. We first measure the flux in elliptical apertures with a Kron factor of $k = 1.2$ (Kron 1980). Then, we perform aperture correction for each source, multiplying the ratio of F356W flux within $k = 2.5$ versus $k = 1.2$ apertures. SExtractor++ also provides the F356W half-light radius measurements. More details about the photometric catalogs are presented in J. B. Champagne et al. (2024, in preparation).

For NIRCam WFSS data, we subtract the $1/f$ noise only along columns. The median background models for WFSS are constructed using all available ASPIRE observations obtained at similar times and are scaled and subtracted from individual WFSS exposures. The WCS of individual exposures is first aligned using the `CALWEBB` pipeline. We then measure the astrometric offsets between the direct images and the fully calibrated F356W-band mosaic, which are added to the spectral tracing model as described below. The spectral tracing models, dispersion models, and sensitivity functions are constructed as described in Sun et al. (2023). The spectral tracing model and the sensitivity functions used in this work are updated using the spectral traces of point sources observed in the LMC field (PID #1076) and Cycle 1 calibration programs (PIDs #1536, #1537, #1538), respectively. We construct and stack the 2D spectra for each source, using 2D spectra from individual exposures that are registered to a common wavelength and spatial grid following the algorithms in `PypeIt` (Prochaska et al. 2020). The pixel scales for the 2D spectra and 1D spectra described below are both resampled to be 10 Å pixel^{-1}.

We first extract 1D spectra using the optimal extraction algorithms and remove the background and continuum using median filters (see Wang et al. 2023 for details). These continuum-removed 1D spectra are used for the initial emission-line identification. After identifying the Hα emitter candidates, we re-extract the 1D spectra for our analysis, without continuum removal. For those with contaminated 2D spectra, we mask regions of $\pm 5000\,\mathrm{km\,s^{-1}}$ around the Hα emission to avoid oversubtraction around the broad wing. We then run median filters iteratively along each row of the 2D spectra to construct continuum maps. We re-extract 1D spectra from these continuum-removed 2D spectra using the optimal extraction algorithms. For samples whose 2D grism spectra are not contaminated by nearby bright sources, we re-extract the 1D spectra based on their original grism data.

2.2. Sample Selection

We systematically search for BHAEs in the 25 ASPIRE fields over a total area of 275 arcmin^2. We select compact red sources first with the following morphology and color cut:

1. F356W half-light radius $< 0.''2$;
2. F200W $-$ F356W > 0.75 mag.

The first requirement for compactness ensures that the source morphology does not broaden the Hα line profiles during the dispersion of grism spectra. The second criterion describes the F356W excess boosted by the strong Hα emission line. We define the color cut based on the broad Hα sample in Matthee et al. (2023). We then perform an emission-line search for all the photometrically selected red compact sources and select objects with strong emission lines at a signal-to-noise ratio (S/N) of integrated line fluxes greater than five. Careful visual inspection is performed to remove artifacts in the imaging and grism data, false detection by the search algorithms, and misidentified lines from contamination of other sources along the dispersion direction. We then fit the line profiles of the emitter candidates with single-Gaussian and two-component Gaussian models. BHAEs are identified in two cases: (i) a single-Gaussian model can well describe the line profile, and it has an FWHM $> 1000\,\mathrm{km\,s^{-1}}$; or (ii) the two-component model with an FWHM $> 1000\,\mathrm{km\,s^{-1}}$ broad component performs better, resulting in $|\chi^2_{\rm red} - 1|$ at least 0.5 smaller than that of single-Gaussian models. The spectroscopic selection can be summarized as follows:

1. emission lines with S/N of integrated line fluxes > 5;
2. robust broad components with FWHM$_{\rm broad}$ $> 1000\,\mathrm{km\,s^{-1}}$.

To test our selection criteria, we generate a mock spectrum assuming a source with an effective radius of 0.″2 and a single emission line with an intrinsic FWHM of $500\,\mathrm{km\,s^{-1}}$. The mock emission line in the dispersed spectrum, broadened by both the line-spread function of NIRCam WFSS and the source morphology, displays a Gaussian profile with FWHM of $715\,\mathrm{km\,s^{-1}}$. This suggests that with flux radii $< 0.''2$ and FWHMs of Hα broad components $> 1000\,\mathrm{km\,s^{-1}}$, the H$\alpha$ of our selected BHAE should have intrinsically broad lines.

We finally identify a total of 16 BHAEs in the 25 ASPIRE fields. Figure 1 presents our selection criteria and the 16 selected BHAEs. Their basic properties are listed in Table 1. We note that our selection does not rely on the SED shape of sources (e.g., Greene et al. 2024). We specifically select compact, point-source-like BHAEs, rather than selecting all BHAEs from a complete Hα emitter sample. The constraint of compactness maximizes the purity of our BHAE sample.

3. Analyses and Results

In this section, we present our analyses and results on a sample of 16 ASPIRE BHAEs. We describe the properties of the broad Hα emission lines in Section 3.1 and derive the BH masses and bolometric luminosities in Section 3.2. The UV and optical continuum slopes are discussed in Section 3.3. Finally, we study the morphology and Hα LF of BHAEs in Sections 3.4 and 3.5.

3.1. Broad Hα Emission

As described in Section 2.2, we fit the extracted 1D spectra with two-component Gaussian models for all 16 BHAEs. We do not impose any limits on the FWHM of the narrow-component Gaussian. Figures 2 and 3 display the 16 BHAEs and their best-fit line profiles. The measurements are presented in Table 2. Among them, J0430M1445-BHAE-1 and J0923P0402-BHAE-1 have two broad components, both with FWHM $> 1000\,\mathrm{km\,s^{-1}}$. The broad-line H$\alpha$ emission is often not adequately modeled as a single Gaussian (Shen et al. 2011). We measure the FWHMs and luminosity of their entire Hα emission for BH mass estimates. J0923P0402-BHAE-1, J1526M2050-BHAE-1, and J1526M2050-BHAE-3 show significantly blueshifted narrow absorption features of the Hα emission peaks (see the third-to-last and second-to-last panels of Figure 2 and the first panel of Figure 3). Similar features were also found in Matthee et al. (2023) and are interpreted as

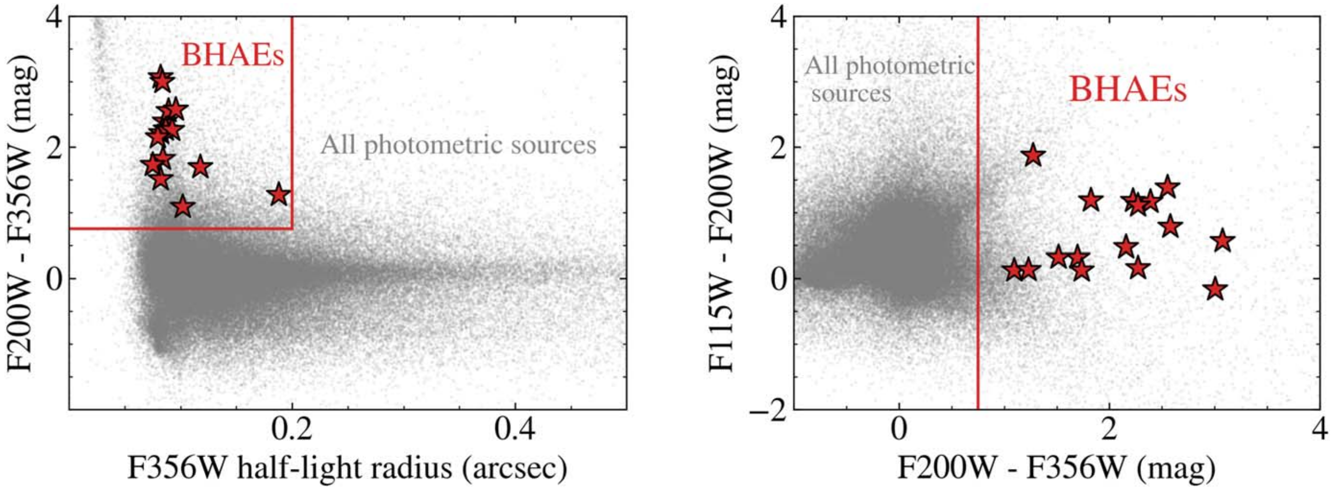

Figure 1. The selection criteria of ASPIRE BHAE (red stars) among all photometric sources in the 25 ASPIRE fields (gray dots). We label the applied color cut and size cut as red lines.

Table 1
The Coordinate, Redshift, and AB Magnitude in F356W of the 16 LRDs in the ASPIRE Fields

ID	R.A.	Decl.	z	F356W mag
J0109M3047-BHAE-1	17.4772	−30.8353	4.3600 ± 0.0006	24.647 ± 0.008
J0218P0007-BHAE-1	34.6950	0.0874	4.2291 ± 0.0004	24.459 ± 0.011
J0224M4711-BHAE-1	36.0952	−47.2007	4.0639 ± 0.0003	24.710 ± 0.014
J0229M0808-BHAE-1	37.4083	−8.1459	4.3653 ± 0.0002	24.804 ± 0.018
J0229M0808-BHAE-2	37.3964	−8.1954	5.0369 ± 0.0002	25.074 ± 0.018
J0430M1445-BHAE-1	67.6898	−14.7873	4.0947 ± 0.0003	23.398 ± 0.004
J0910M0414-BHAE-1	137.7143	−4.2213	4.9102 ± 0.0003	24.878 ± 0.018
J0923P0402-BHAE-1	140.9658	4.0545	4.8688 ± 0.0005	23.815 ± 0.005
J1526M2050-BHAE-1	231.6589	−20.8692	4.1573 ± 0.0005	23.860 ± 0.006
J1526M2050-BHAE-2	231.6513	−20.8566	4.8708 ± 0.0007	25.181 ± 0.026
J1526M2050-BHAE-3	231.6710	−20.8434	4.8751 ± 0.0005	25.477 ± 0.018
J2002M3013-BHAE-1	300.6666	−30.1814	4.9461 ± 0.0003	24.091 ± 0.003
J2132P1217-BHAE-1	323.1515	12.3108	4.9250 ± 0.0001	24.852 ± 0.022
J2232P2930-BHAE-1	338.2275	29.4940	4.1349 ± 0.0003	23.390 ± 0.008
J2232P2930-BHAE-2	338.2381	29.5225	4.4693 ± 0.0002	25.905 ± 0.014
J2232P2930-BHAE-3	338.2325	29.5094	4.7061 ± 0.0003	25.324 ± 0.012

Note. The redshift uncertainties are determined from the uncertainties in Gaussian fitting of Hα. The uncertainties in F356W magnitude are based on measurements. However, we apply an uncertainty floor of $\Delta m = 0.05$ when calculating the continuum slope.

narrow Hα absorption. Whether the features originate from Hα absorption or just complexes of multicomponent emission lines remains uncertain. In this work, we assume that they are caused by Hα absorption and fit them as a single Gaussian. We adopt the total Hα luminosity values without absorption as the intrinsically emitted Hα luminosity for $L_{\mathrm{H}\alpha,\mathrm{total}}$. We note that the broad Hα fit is robust under the inclusion of the absorption, and we exclude this component when measuring the broad Hα components.

Figure 4 presents the properties of broad Hα emission of ASPIRE BHAEs, together with literature high-redshift BHAEs (Harikane et al. 2023; Maiolino et al. 2023; Matthee et al. 2023; Greene et al. 2024) and low-redshift type 1 quasars observed by the Sloan Digital Sky Survey (SDSS; Wu & Shen 2022). We only present SDSS quasars at $z < 0.6$ whose Hα lines are observable in SDSS spectra. As shown in the left panel of Figure 4, the FWHMs and luminosities of the broad Hα emission of BHAEs are distributed similarly to those of type 1 quasars. This implies that BHAEs likely have BLRs similar to those of typical low-redshift type 1 quasars. On the other hand, the fraction of Hα flux in the broad components, with a median of 0.70, as shown in the middle panel of Figure 4, is generally lower than that in most of the low-redshift quasars (median 0.93). This indicates that the contributions from the narrow-line regions (NLRs) or host galaxies in these BHAEs to the total Hα luminosity (median $L_{\mathrm{H}\alpha,\mathrm{narrow}}/L_{\mathrm{H}\alpha,\mathrm{total}} = 0.30$) are higher than those of low-redshift type 1 quasars (median $L_{\mathrm{H}\alpha,\mathrm{narrow}}/L_{\mathrm{H}\alpha,\mathrm{total}} = 0.07$). If the narrow H$\alpha$ components largely originate from the host galaxies, the high values of $L_{\mathrm{H}\alpha,\mathrm{narrow}}/L_{\mathrm{H}\alpha,\mathrm{total}}$ suggest a higher star formation rate in the host galaxies of these BHAEs than those in typical low-redshift quasars. The right panel of Figure 4 shows that $L_{\mathrm{H}\alpha,\mathrm{broad}}/L_{\mathrm{H}\alpha,\mathrm{total}}$ generally increases with $L_{\mathrm{H}\alpha,\mathrm{broad}}$. It is likely a natural outcome of dust obscuration within BLRs, where BLRs of BHAEs with lower $L_{\mathrm{H}\alpha,\mathrm{broad}}$ are subject to greater attenuation.

3.2. Black Hole Mass and Bolometric Luminosity

We estimate the bolometric luminosity (L_{bol}) and BH mass (M_{BH}) based on the broad Hα emission line as done in recent

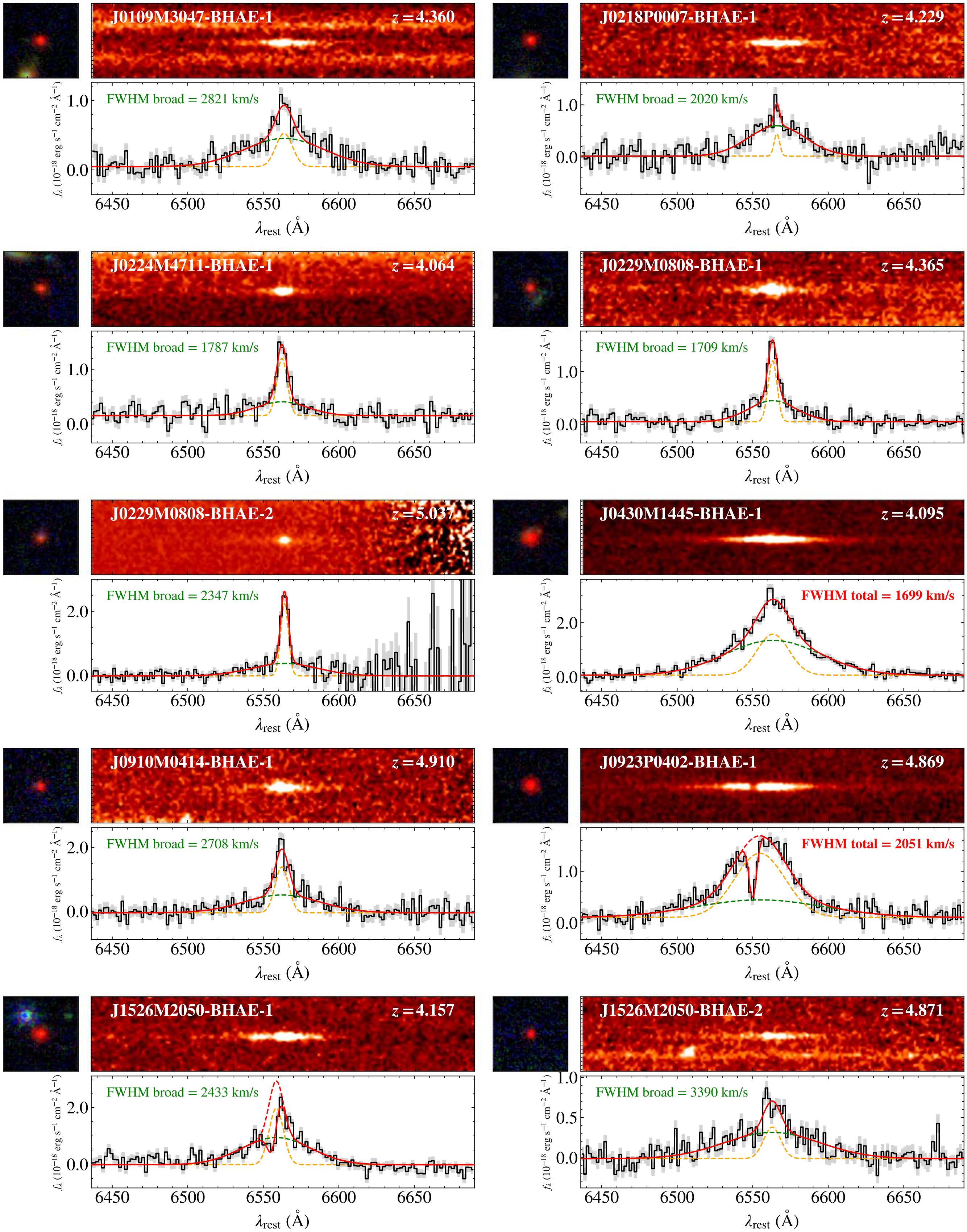

Figure 2. The BHAEs identified in 25 ASPIRE fields. For each source, the upper left panel shows a 2″ × 2″ RGB thumbnail composed of JWST/NIRCam F356W, F200W, and F115W images. The top panel shows the 2D grism spectrum with continuum and background removed. The bottom panel is the optimally extracted 1D spectrum (black) and the corresponding error spectrum (gray shaded region). We show the total best-fit line profile as the red solid line, the narrow component as the orange dashed line, and the broad component as the green dashed line. For J0923P0402-BHAE-1, J1526M2050-BHAE-1, and J1526M2050-BHAE-3, we also show the Hα profiles without the absorption features as the red dashed lines. J0923P0402-BHAE-1 and J0430M1445-BHAE-1 present two broad Hα components with FWHM $>$ 1000 km s^{-1}. We label the FWHMs of their total Hα emission, which are used to estimate the BH masses.

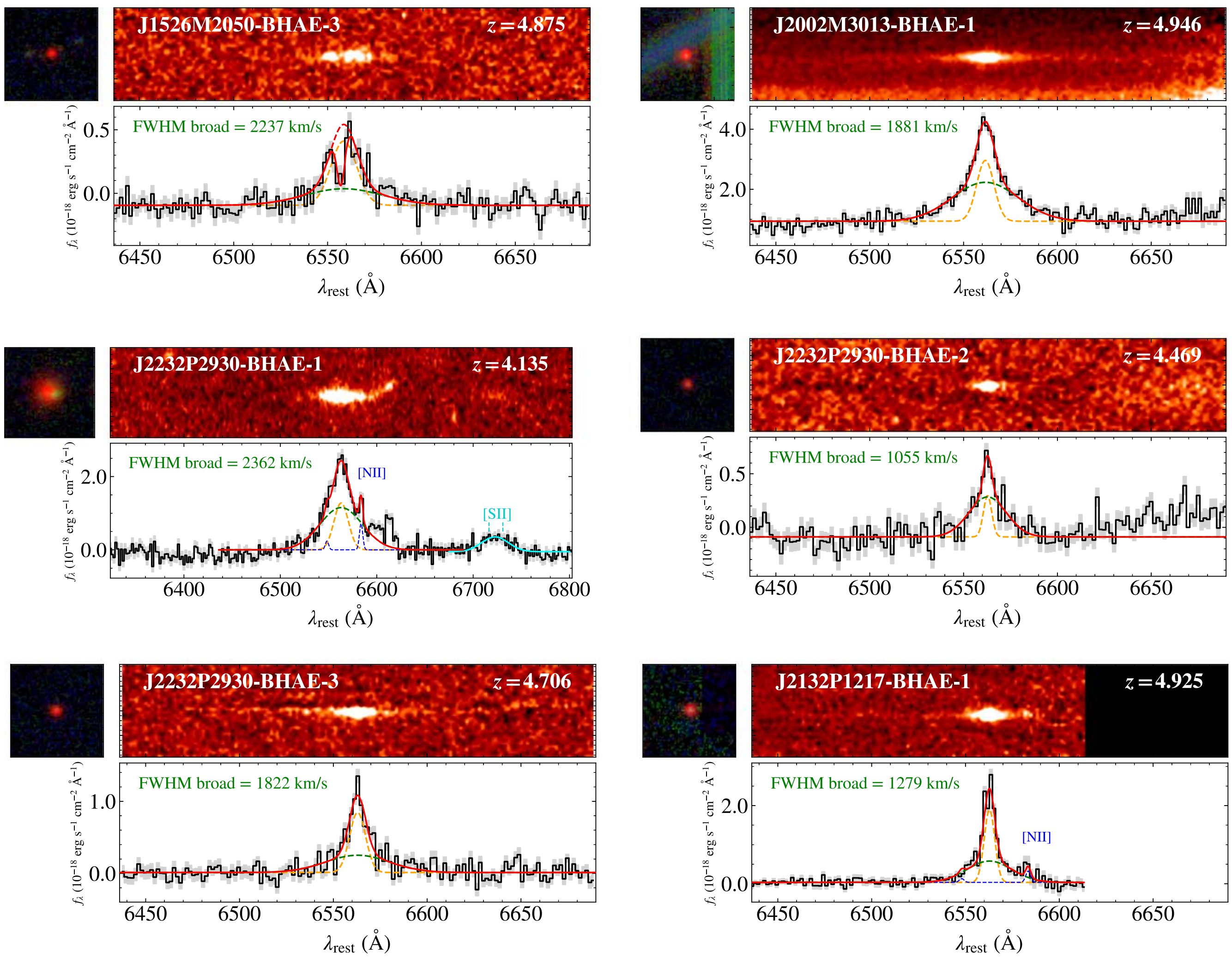

Figure 3. Same as Figure 2. For J2232P2930-BHAE-1, we also show the [N II]$\lambda\lambda$6548, 6583 emission lines in blue and [S II]$\lambda\lambda$6718, 6732 in cyan. In the 2D spectrum of J2232P2930-BHAE-1, the emission on its top right originates from a companion Hα emitter at the same redshift (Companion-2; see Section 4.2.2).

works (e.g., Harikane et al. 2023; Matthee et al. 2023). Following Reines et al. (2013), we estimate $M_{\rm BH}$ as

$$\log_{10}(M_{\rm BH}/M_\odot) = 6.57 + \log_{10}(\epsilon) + 0.47\log_{10}(L_{\rm H\alpha,broad}/10^{42}\ {\rm erg\ s^{-1}}) + 2.06\log_{10}({\rm FWHM_{broad}}/10^3\ {\rm km\ s^{-1}}). \quad (1)$$

The geometric correction factor related to the BLR, ϵ, is assumed to be 1.075 (Reines & Volonteri 2015). The BH estimator has an intrinsic uncertainty of 0.5 dex (Reines & Volonteri 2015). Note that, limited by our wavelength coverage, we derive the estimated $M_{\rm BH}$ values here without dust attenuation correction, as done in Matthee et al. (2023); the $M_{\rm BH}$ values could be even higher after correcting for the dust attenuation.

We derive $L_{\rm bol}$ by adopting the relation between the rest-frame 5100 Å luminosity (L_{5100}) and the AGN-induced Hα luminosity in Greene & Ho (2005), with the bolometric correction in Richards et al. (2006):

$$L_{5100} = 10^{44}(L_{\rm H\alpha}/5.25 \times 10^{42}{\rm erg\ s^{-1}})^{1/1.157}{\rm erg\ s^{-1}}$$
$$L_{\rm bol} = 10.33 \times L_{5100}, \quad (2)$$

where $L_{\rm H\alpha}$ in Equation (2) should include Hα from both AGN NLRs and BLRs in principle. Since it is still not clear whether the narrow Hα components of BHAEs originate from AGN NLRs or the host galaxies, we use $L_{\rm H\alpha,broad}$ as the input. The $L_{\rm bol}$ could be higher if the dust attenuation correction is applied or the contribution from AGN NLRs is included. We discuss the caveat of the $L_{\rm bol}$ estimator in Section 4.1. The Eddington ratio $\lambda_{\rm Edd}$ is defined as $L_{\rm bol}/L_{\rm Edd}$, where $L_{\rm Edd}$ is the theoretical maximum luminosity achievable when radiation pressure and gravity are balanced in a spherical geometry. We calculate $\lambda_{\rm Edd}$ following Trakhtenbrot et al. (2011):

$$\lambda_{\rm Edd} = \frac{L_{\rm bol}/{\rm erg\ s^{-1}}}{1.5 \times 10^{38}M_{\rm BH}/M_\odot}. \quad (3)$$

We list the derived physical properties of BHAEs in Table 3. Figure 5 shows the estimated $M_{\rm BH}$ and $L_{\rm bol}$ of ASPIRE BHAEs, together with literature BHAEs[31] and SDSS quasars. To display the effect of dust attenuation, we also show arrows associated with each BHAE. The lengths of the arrows indicate

[31] We note that the $L_{\rm bol}$ estimator is different in Harikane et al. (2023), the central values of $L_{\rm bol}$ are estimated using both the narrow and broad Hα components, the lower limits of $L_{\rm bol}$ are estimated using the broad Hα only, and the upper limits are estimated under the assumption of type 2 AGNs with [O III] and Hβ. In this work, we use the broad Hα only, following Matthee et al. (2023).

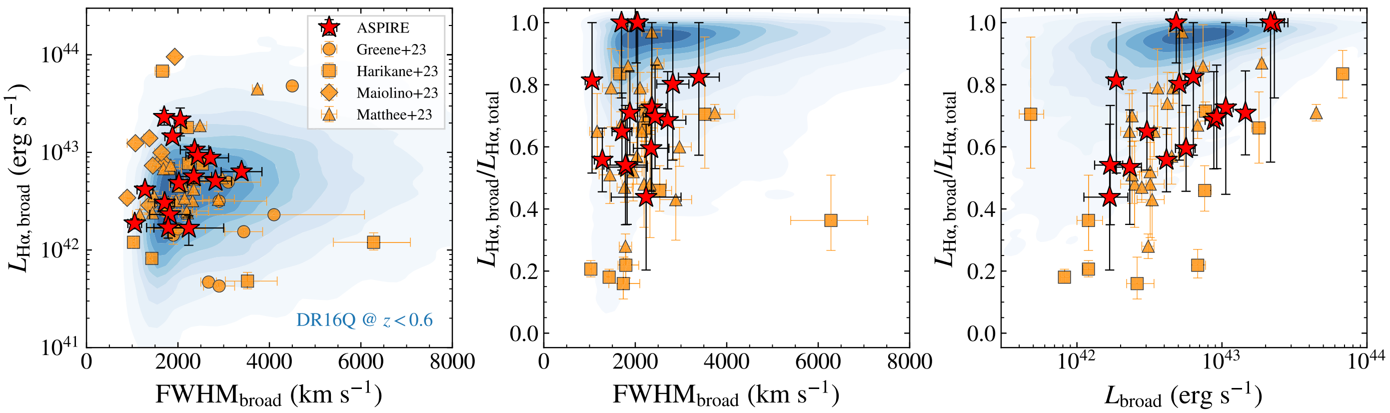

Figure 4. The properties of broad Hα emission lines of BHAEs. In the left panel, we show the relation between the FWHM and the luminosity of the broad Hα components. We show the fraction of Hα luminosity in the broad components as a function of the broad Hα FWHMs in the middle panel and as a function of the broad Hα luminosity in the right panel. The ASPIRE BHAEs are denoted as red stars. We present the measurements of literature BHAEs in Greene et al. (2024; $4.5 < z < 8.5$; orange circle), Harikane et al. (2023; $4 < z < 7$; orange square), Maiolino et al. (2023; $4 < z < 7$; orange diamond), and Matthee et al. (2023; $4.2 < z < 5.5$; orange triangle). The blue shaded region denotes the distribution of $z < 0.6$ quasars with Hα emission lines in SDSS spectra (Wu & Shen 2022).

Table 2
The Hα Properties of LRDs in the ASPIRE Fields

ID	FWHM$_{\mathrm{broad}}$ (km s^{-1})	FWHM$_{\mathrm{narrow}}$ (km s^{-1})	$L_{\mathrm{H}\alpha,\mathrm{broad}}$ (10^{42} km s^{-1})	$L_{\mathrm{H}\alpha,\mathrm{total}}$ (10^{42} km s^{-1})	EW$_{\mathrm{H}\alpha,\mathrm{broad}}$ (Å)
J0109M3047-BHAE-1	2821 ± 351	559 ± 119	5.08 ± 0.55	6.33 ± 1.81	630 ± 119
J0218P0007-BHAE-1	2020 ± 184	…	4.84 ± 0.44	4.84 ± 0.44	476 ± 53
J0224M4711-BHAE-1	1787 ± 472	306 ± 50	1.70 ± 0.37	3.13 ± 0.87	227 ± 53
J0229M0808-BHAE-1	1709 ± 217	253 ± 31	3.04 ± 0.32	4.68 ± 0.74	405 ± 56
J0229M0808-BHAE-2	2347 ± 388	202 ± 19	5.65 ± 0.88	9.50 ± 1.64	818 ± 189
J0430M1445-BHAE-1	1699 ± 16	…	22.97 ± 3.94	22.97 ± 3.94	1206 ± 125
J0910M0414-BHAE-1	2708 ± 397	444 ± 53	8.79 ± 1.14	12.82 ± 2.41	2333 ± 1308
J0923P0402-BHAE-1	2051 ± 132	…	21.63 ± 6.87	21.63 ± 6.87	1121 ± 240
J1526M2050-BHAE-1	2433 ± 260	471 ± 63	9.20 ± 0.80	13.21 ± 2.95	656 ± 105
J1526M2050-BHAE-2	3390 ± 446	572 ± 121	6.35 ± 0.79	7.70 ± 2.14	1493 ± 655
J1526M2050-BHAE-3	2237 ± 763	719 ± 146	1.68 ± 0.56	3.84 ± 1.60	345 ± 149
J2002M3013-BHAE-1	1881 ± 166	459 ± 52	14.52 ± 1.11	20.47 ± 3.58	1081 ± 270
J2132P1217-BHAE-1	1279 ± 173	235 ± 23	4.14 ± 0.43	7.43 ± 1.12	480 ± 80
J2232P2930-BHAE-1	2363 ± 310	780 ± 134	10.62 ± 1.32	14.63 ± 5.32	436 ± 79
J2232P2930-BHAE-2	1055 ± 149	136 ± 51	1.87 ± 0.22	2.30 ± 0.80	733 ± 182
J2232P2930-BHAE-3	1822 ± 442	417 ± 61	2.31 ± 0.47	4.33 ± 1.21	469 ± 133

Note. FWHM$_{\mathrm{broad}}$ and FWHM$_{\mathrm{narrow}}$ are the FHWMs measured for the broad and narrow Hα components, respectively. $L_{\mathrm{H}\alpha,\mathrm{broad}}$ is the Hα luminosity of the broad component, and $L_{\mathrm{H}\alpha,\mathrm{total}}$ is the Hα luminosity of the total Hα emission without absorption. EW$_{\mathrm{H}\alpha,\mathrm{broad}}$ is the rest-frame equivalent width of the broad Hα emission. The narrow Hα component of J0218P0007-BHAE-1 is unresolved, and thus we do not show its FWHM$_{\mathrm{narrow}}$. J0430M1445-BHAE-1 and J0923P0402-BHAE-1 exhibit two Gaussian components, both with FWHM > 1000 km s^{-1}, so we measure the FWHM and luminosity of all the Hα emission lines as the FWHM$_{\mathrm{broad}}$ and L_{broad}.

changes in M_{BH} and L_{bol}, with A_V varying from 0 to 2. The M_{BH} of ASPIRE BHAEs ranges from 10^7 to 10^8 $M_\odot$, comparable to those of low-redshift quasars. The Hα converted L_{bol} of BHAEs implies that the BHs are accreting at $\lambda_{\mathrm{Edd}} \approx 0.07$–$0.47$, with a median λ_{Edd} of 0.17. The λ_{Edd} of BHAEs are comparable to or slightly lower than those of $z > 5$ quasars (median values $\sim$0.3–0.8; Shen et al. 2019; Farina et al. 2022; Mazzucchelli et al. 2023).

3.3. UV and Optical Slopes

The large difference in UV and optical slopes (β_{UV}, β_{opt}, defined as $f_\lambda = \lambda^\beta$) is one of the primary puzzles about the nature of so-called LRDs (e.g., Killi et al. 2023; Matthee et al. 2023). We approximate β_{UV} for all ASPIRE BHAEs by fitting the F115W and F200W photometry with a power law, which spans over rest frame 2000–3600 Å at $z \sim 4.5$. We assume that there are no strong emission lines in the two filters. The values of β_{opt} are estimated using F200W and emission-line-subtracted F356W photometry. We estimated the uncertainties of β_{UV} and β_{opt} through the Monte Carlo (MC) method. This involved generating mock photometry based on the measurements and uncertainties and then recalculating the beta values 10^4 times. An uncertainty floor of 0.05 mag is applied. The derived slopes are listed in Table 3.

Figure 6 displays the relation between β_{opt} and β_{UV}, the fraction of Hα flux in the broad component $L_{\mathrm{H}\alpha,\mathrm{broad}}/L_{\mathrm{H}\alpha,\mathrm{total}}$, and M_{BH}. Most of the BHAEs show redder β_{opt} than β_{UV}, except J2232P2930-BHAE-1. J2232P2930-BHAE-1 is the most extended source in our sample with bright and diffuse Hα emission (see Section 4.2.2 for more details). We do not see a correlation between β_{opt} and $L_{\mathrm{H}\alpha,\mathrm{broad}}/L_{\mathrm{H}\alpha,\mathrm{total}}$ in ASPIRE BHAEs. The Kendall's τ correlation analysis on

Table 3
The Black Hole and Galaxy Properties of LRDs in the ASPIRE Fields

ID	$M_{\rm UV}$	$\beta_{\rm UV}$	$\beta_{\rm opt}$	$\log M_{\rm BH}$	$\log L_{\rm bol}$
J0109M3047-BHAE-1	-17.21 ± 0.31	-0.07 ± 0.74	1.08 ± 0.32	7.86 ± 0.11	$45.00^{+0.04}_{-0.04}$
J0218P0007-BHAE-1	-17.39 ± 0.30	0.05 ± 0.69	1.08 ± 0.16	7.55 ± 0.08	$44.98^{+0.03}_{-0.04}$
J0224M4711-BHAE-1	-17.43 ± 0.19	-0.00 ± 0.40	0.54 ± 0.17	7.23 ± 0.24	$44.59^{+0.08}_{-0.09}$
J0229M0808-BHAE-1	-19.15 ± 0.10	-1.47 ± 0.23	0.10 ± 0.18	7.31 ± 0.12	$44.81^{+0.04}_{-0.04}$
J0229M0808-BHAE-2	-20.07 ± 0.04	-1.79 ± 0.15	-1.32 ± 0.32	7.72 ± 0.15	$45.04^{+0.05}_{-0.06}$
J0430M1445-BHAE-1	-17.68 ± 0.18	0.35 ± 0.38	1.19 ± 0.24	7.72 ± 0.04	$45.57^{+0.06}_{-0.07}$
J0910M0414-BHAE-1	-18.98 ± 0.13	-1.74 ± 0.40	-0.70 ± 1.18	7.94 ± 0.13	$45.21^{+0.05}_{-0.05}$
J0923P0402-BHAE-1	-18.62 ± 0.13	-1.04 ± 0.41	1.73 ± 0.61	7.87 ± 0.09	$45.55^{+0.11}_{-0.14}$
J1526M2050-BHAE-1	-18.04 ± 0.15	-0.13 ± 0.35	0.87 ± 0.26	7.85 ± 0.10	$45.22^{+0.03}_{-0.03}$
J1526M2050-BHAE-2	-18.43 ± 0.27	-2.32 ± 0.93	1.19 ± 0.96	8.07 ± 0.12	$45.09^{+0.04}_{-0.05}$
J1526M2050-BHAE-3	-17.15 ± 0.27	-0.75 ± 0.79	1.23 ± 0.62	7.43 ± 0.31	$44.59^{+0.11}_{-0.15}$
J2002M3013-BHAE-1	-20.86 ± 0.03	-1.77 ± 0.12	-1.45 ± 0.46	7.71 ± 0.08	$45.40^{+0.03}_{-0.03}$
J2132P1217-BHAE-1	-19.53 ± 0.09	-1.46 ± 0.31	-0.51 ± 0.27	7.11 ± 0.12	$44.93^{+0.04}_{-0.04}$
J2232P2930-BHAE-1	-18.15 ± 0.15	1.17 ± 0.32	-0.47 ± 0.25	7.85 ± 0.12	$45.28^{+0.04}_{-0.05}$
J2232P2930-BHAE-2	-18.37 ± 0.10	-1.79 ± 0.27	-0.06 ± 0.43	6.78 ± 0.13	$44.63^{+0.04}_{-0.05}$
J2232P2930-BHAE-3	-18.08 ± 0.17	-1.20 ± 0.47	0.54 ± 0.39	7.31 ± 0.22	$44.71^{+0.07}_{-0.08}$

Note. $M_{\rm UV}$ is the absolute UV magnitude at the rest frame 1500 Å. $\beta_{\rm UV}$ is the UV slope derived from the F115W and F200W magnitudes. $\beta_{\rm opt}$ is the optical slope derived from the F200W and F356W magnitudes, where we subtract the Hα emission flux in the F356W to obtain the continuum flux. The BH mass and bolometric luminosity values have been calculated from the observed Hα emission without dust correction; hence, their intrinsic values might be higher.

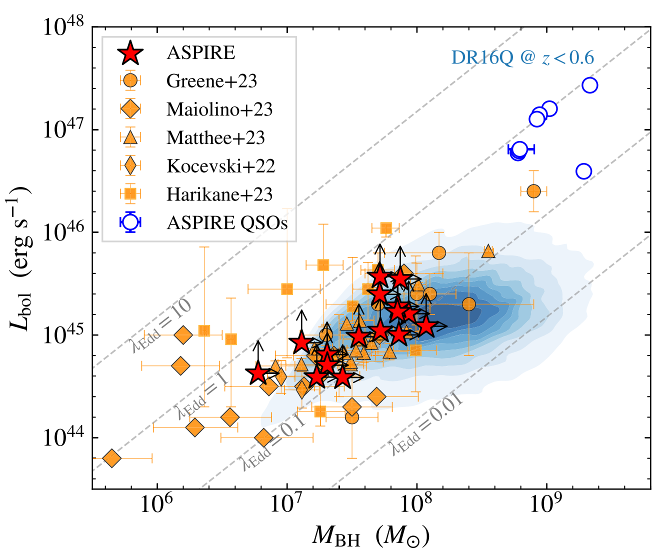

Figure 5. BH mass ($M_{\rm BH}$) vs. bolometric luminosity ($L_{\rm bol}$). The red stars show the estimates in this work. The lengths of arrows indicate the changes of $M_{\rm BH}$ and $L_{\rm bol}$ when A_V varies from 0 to 2. The orange squares, thin diamonds, triangles, diamonds and circles show the estimates from the literature BHAEs in Harikane et al. (2023), Kocevski et al. (2023), Maiolino et al. (2023), Matthee et al. (2023), and Greene et al. (2024), respectively. Note that the $L_{\rm bol}$ estimator used in Harikane et al. (2023) is different as discussed in Section 3.2. We present the distribution of low-redshift ($z < 0.6$) quasars from Wu & Shen (2022) as the blue shaded region, with the depth demonstrating their number density. The blue-edged circles are measurements for $z > 6.5$ quasars, deriving $M_{\rm BH}$ from Hβ emission lines and $L_{\rm bol}$ from L_{5100}. We draw equal Eddington ratio lines (gray dashed) of $\lambda_{\rm Edd} = 0.01$, 0.1, 1, and 10.

ASPIRE BHAEs yields a correlation coefficient of $r = 0.27 \pm 0.22$ and p-value of $0.2^{+0.4}_{-0.2}$. Likewise, no strong correlation can be concluded from the $\beta_{\rm opt}$–$M_{\rm BH}$ relation in ASPIRE BHAEs. The Kendall's τ correlation analysis between $\beta_{\rm opt}$ and $\log M_{\rm BH}$ of ASPIRE BHAEs shows $r = 0.19^{+0.18}_{-0.17}$ and a p-value of $0.3^{+0.4}_{-0.3}$. Our results are not consistent with the tight correlation seen in Matthee et al. (2023), who interpret the correlations as transitions from a star-formation-dominated phase with small $M_{\rm BH}$ to a dusty-AGN-dominated phase with massive BHs. Our results suggest that the evolutionary track of these high-redshift AGNs might be nonlinear or not identical among individual objects. However, we caution that the $\beta_{\rm UV}$ and $\beta_{\rm opt}$ values in both this work and Matthee et al. (2023) are calculated based on only two broad bands. The UV and optical continuum shapes may not be simple power laws, so the estimates with two broad bands can be highly uncertain. Future JWST/NIRSpec Prism and Grating spectra of larger BHAE samples are required to test the evolutionary scenario depicted in Matthee et al. (2023).

3.4. Morphology

Limited by the depth of ASPIRE observations, it is difficult to identify the host or companion galaxies of individual BHAEs. To detect possible extended emission, we stack the images of 14 BHAEs in the ASPIRE sample. Among the 16 total ASPIRE BHAEs, J2232P2930-BHAE-1 is not included because it is a composite system presenting significant extended Hα emission (Section 4.2.2), and J2002M3013-BHAE-1 is not included because its image is severely contaminated by bright spikes of saturated stars nearby. We generate $3'' \times 3''$ cutouts of the three bands for each BHAE and normalize the images to the value of the central brightest pixels. We stack the normalized cutouts and obtain the 3σ clipped mean. We use the median value of the outskirt 10 pixels in the stack of each band as the background level and subtract it from the final stack. For cross-checking, we also perform point-spread function (PSF) subtraction for each AGN using `Galfit` (Peng et al. 2002). The PSF models in each band are built by stacking Gaia stars in the 23 ASPIRE fields (see more details in J. B. Champagne et al. 2024, in preparation). We subtract the PSF models within the central 8 pixel × 8 pixel regions of the cutouts. The PSF-subtracted images are stacked in the same way, normalized using the central brightest pixels

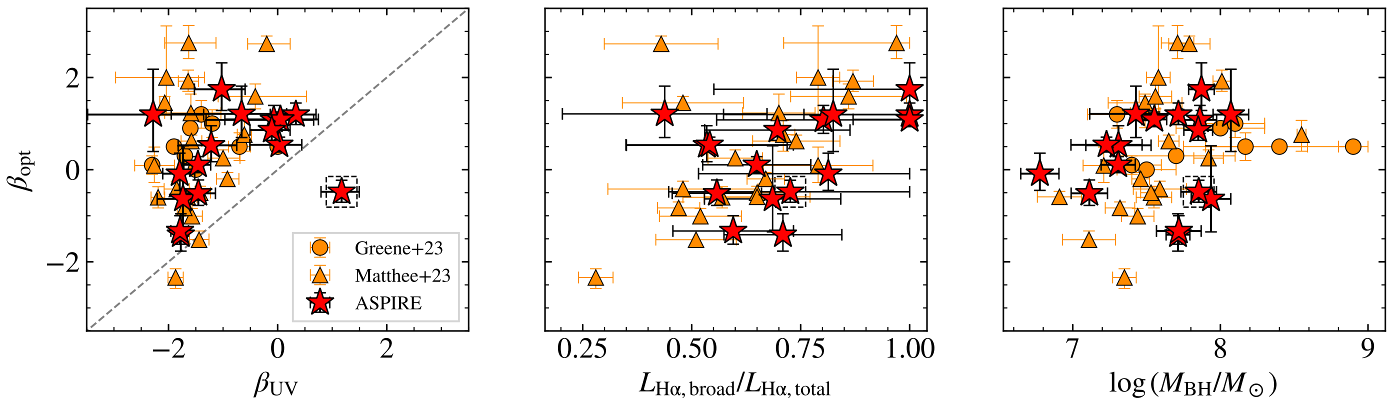

Figure 6. The relation between the optical slope ($\beta_{\rm opt}$) and UV slope ($\beta_{\rm UV}$), the fraction of Hα flux in the broad components ($L_{\rm H\alpha,broad}/L_{\rm H\alpha,total}$), and BH mass ($M_{\rm BH}$). The measurements for ASPIRE BHAEs are denoted as red stars. The literature BHAEs in Greene et al. (2024) and Matthee et al. (2023) are shown as orange circles and triangles, respectively. We label the source J2232P2930-BHAE-1 using a dashed square. More details about it are presented in Section 4.2.2.

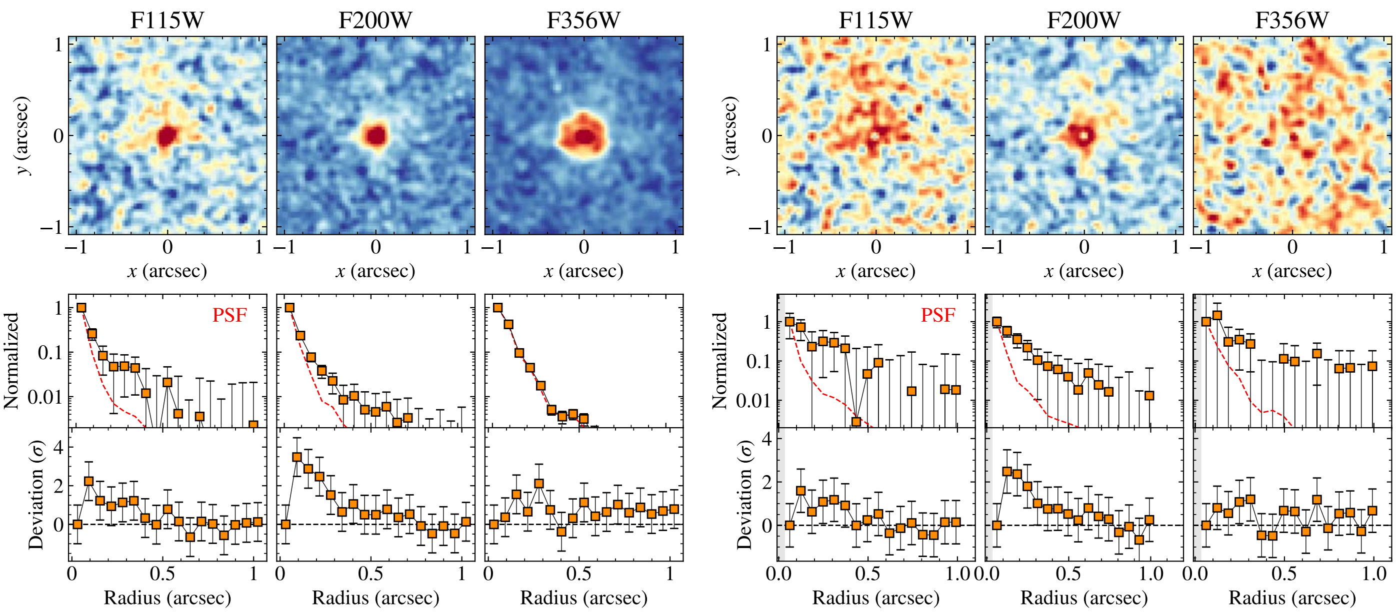

Figure 7. Left: stack of images of 13 BHAEs in NIRCam F115W, F200W, and F356W, normalized to the value of central pixels. The top panel shows the $3'' \times 3''$ stack of each band. In the middle panel, the radial profiles of the AGN stacks are shown as orange squares, and the radial profiles of PSFs are shown as red dashed lines. The bottom panel shows the deviations of the stacked AGN radial profiles from the corresponding PSFs as defined in Equation (4). Right: the stack of PSF-subtracted images of 13 BHAEs, also normalized by the value of central pixels in the original images. The radial profiles of the AGN stacks and the deviation from the PSFs are shown in the middle and bottom panels, respectively. The calculation of PSF-subtracted radial profiles starts at $r = 1$ pixel ($0\overset{''}{.}031$), to avoid the 2 pixel $\times$ 2 pixel oversubtracted region in the centers. The $r < 1$ pixel ranges are shaded gray in the middle and bottom panels.

of the original cutouts. We calculate the radial profiles of the two stacked versions. The calculation of PSF-subtracted radial profiles starts at $r = 1$ pixel ($0\overset{''}{.}031$), to avoid the 2 pixel $\times$ 2 pixel oversubtracted region in the centers. To compare the radial profiles of stacked images with the PSF profiles, we normalize all the profiles to their maximum values, so that the maximum values are unity at the minimum radius. To quantify the deviation of stacked images from the PSF shape, we define the deviation as

$$\sigma(r) = \frac{S(r) - S_{\rm PSF}(r)}{\delta S(r)}, \quad (4)$$

where $\sigma(r)$ is the extent of the $S(r)$ profile deviation from the PSF profile $S_{\rm PSF}(r)$ with respect to the uncertainty $\delta S(r)$. For instance, $\sigma = 1$ means that the radial profile $S(r)$ deviates from the PSF shape at a level of 1σ.

Figure 7 shows the stacked images of BHAEs and the corresponding radial profiles. With the longest exposure time in F200W, both the F200W stack of original images and PSF-subtracted images present extended morphology. The radial profiles of the two F200W stacked images both deviate significantly from the shape of PSFs, with $\sigma \approx 3.5$ at $0\overset{''}{.}1$ and $\sigma \approx 1$ at $0\overset{''}{.}4$. The stacked F200W extends to ~2.6 physical kpc (pkpc) at $z = 4.5$. The F115W and F356W stacks are also tentatively extended with $\sigma \gtrsim 1$ within $r < 0\overset{''}{.}3$–$0\overset{''}{.}4$. The presence of extended structure in F200W, corresponding to rest frame ~3600 Å at $z \sim 4.5$, is likely caused by the stellar emission from the host galaxies.

3.5. Luminosity Function

The large survey area of the ASPIRE program on 275 arcmin^2 (25 ASPIRE fields) allows us to measure the number density of broad-Hα-line-selected BHAEs at the bright end and reduce the effect of cosmic variance. We do not calculate the UV LF of BHAEs since it is still uncertain whether the UV components of BHAEs originate from the host galaxies or the scattered light from AGNs. Instead, we focus on the Hα LF using the total Hα flux (narrow + broad) directly measured from the observations.

To calculate the total survey volume, we first compute the effective survey area for each BHAE, where the noise levels enable us to reliably identify the broad wing of the Hα emission lines. To do this, we need to ascertain the maximum rms value for the identification of the broad Hα lines. We generate a series of mock 2D grism spectra. We convolve the two-component Gaussian model of each ASPIRE AGN with the line-spread function of NIRCam WFSS along the wavelength axis and the F356W PSF along the spatial axis. We then add noise to the 2D mock spectrum and extract the 1D spectrum using the boxcar algorithm. We fit the extracted 1D spectrum using a single-Gaussian model and a two-component Gaussian model. If the two-component Gaussian model yields an S/N > 3 and a $|\chi^2_{\rm red} - 1|$ value that is 0.1 smaller than that of the single-Gaussian model, the broad Hα line is successfully identified. We progressively increase the noise levels added to the mock 2D spectra until the broad Hα components cannot be characterized. The noise values at this stage are the maximum rms for the broad Hα identification. The survey volume is computed following the procedure in Sun et al. (2023). We define a series of redshifts spanning from 3.6 to 5.1, with Hα emission lines residing at 3–4 μm. We compute the effective sky area based on the spectral tracing and grism dispersion models for a specific redshift and construct the rms maps using continuum-removed WFSS `cal` files. The maximum sky area at this redshift is determined as the area on the rms map with rms noise smaller than the maximum rms for Hα broad-line identification. The maximum survey volume ($V_{\rm max}$) for each BHAE is integrated from the maximum sky area across $z = 3.6$–5.1 over all 25 ASPIRE fields. The median $V_{\rm max}$ for our AGN sample is 911,561 cMpc^3.

The Hα LF of BHAEs is then computed using the direct $1/V_{\rm max}$ method (Schmidt 1968):

$$\Phi(L) = \frac{1}{d\log L}\sum_i \frac{1}{C_i V_{{\rm max},i}}, \quad (5)$$

where L is the Hα luminosity of each LF bin, C_i accounts for the completeness correction, and $V_{{\rm max},i}$ is the maximum survey volume for the ith source. To measure completeness, we randomly draw noise values from the effective rms map as described above. We generate 2D mock grism spectra for each BHAE based on the two Gaussian models, adding the selected rms values. We then re-extract the 1D spectrum following the procedure in Section 2. We run 1000 mock realizations for each BHAE, refitting the two-component Gaussian model to the extracted spectra. The completeness is defined as the fraction of the realizations in which the broad Hα components are successfully characterized according to the criteria mentioned above. Additionally, we perform 1000 MC experiments for each luminosity bin to calculate the uncertainties, propagating the uncertainties of line fluxes to the LF. In each MC run, we account for the Poisson noise associated with small number statistics following the prescription in Gehrels (1986). We also take into account the potential incompleteness caused by the color cut (see Section 2.2). We generate 10^4 mock BHAE optical spectra assuming uniformly distributed $L_{\rm broad}$ in log space with $\log(L_{\rm broad}/{\rm erg\ s^{-1}})$ from 41.5 to 44, $L_{\rm broad}/L_{\rm tot}$ from 0.1 to 1, $\beta_{\rm opt}$ from −2.5 to 2.5, FWHM$_{\rm broad}$ from 1000 to 3000 km s^{-1}, FWHM$_{\rm narrow}$ from 500 to 900 km s^{-1}, F200W magnitude from 25.5 to 27 mag, and redshift within $z = 4$–5. We measure the F200W–F356W color excess for these mock BHAEs. We find that, for the LF of the total Hα emission, the color cut only excludes 8.6% of BHAEs in the faintest Hα luminosity bin ($L_{\rm tot} \approx 10^{42.5}$ erg s^{-1}) and is nearly complete in more luminous bins. For the broad Hα LF, the fraction is 12.6% in the faintest bin ($L_{\rm broad} \approx 10^{42.3}$ erg s^{-1}) and also complete in more luminous bins. This minor incompleteness is insignificant when considering the substantial uncertainty and the completeness correction due to the background rms. We do not correct the incompleteness caused by the color cut because the intrinsic distribution of the physical parameters remains unclear.

Figure 8 shows the Hα LF for ASPIRE BHAEs, and the number density of each Hα luminosity bin is listed in Table 4. The number densities of BHAEs are much lower than those of star-forming galaxies at similar redshifts. The fraction of BHAEs at each luminosity bin is computed as the number density of BHAEs over the number density of Lyman break galaxies as derived in Bollo et al. (2023). The fractions increase strongly with $L_{\rm H\alpha}$, from 2% at $\log(L_{\rm H\alpha}/{\rm erg\ s^{-1}}) \approx 42.5$ to 17% at $\log(L_{\rm H\alpha}/{\rm erg\ s^{-1}}) \approx 43.3$. The most luminous H$\alpha$ emitters include a large portion of broad-line AGNs at $z \approx 4$–5. The rising trend of AGN fraction toward the higher-luminosity end is in agreement with those observed at $z \approx 0.8$–2.2 (Stott et al. 2013; Sobral et al. 2016). To more precisely quantify the AGN fraction at high redshift, deeper spectroscopic observations are required to resolve the broad components in fainter Hα emitters.

To compare the number density of BHAEs with those of quasars and AGNs at similar redshifts, we estimate the bolometric LF of BHAEs by converting their $L_{\rm H\alpha,broad}$ into $L_{\rm bol}$ following Equation (2). The bolometric LF is shown in Figure 9. For comparison, we also convert the broad Hα LF of Matthee et al. (2023) into $L_{\rm bol}$. At the most luminous bin ($L_{\rm bol} \approx 10^{45.5}$ erg s^{-1}), our result is consistent with the extrapolation of the bolometric LF of quasars at $z \sim 4$ but is $\sim$2 × higher than those of quasars at $z \sim 5$, despite the large uncertainty. At the faintest end ($L_{\rm bol} \approx 10^{44.7}$ erg s^{-1}) the number density of BHAEs is approximately 1.6× that of $z \sim 4$ quasars and 3.7 × that of $z \sim 5$ quasars. The underlying BHAE population could have a higher number density with fainter $L_{\rm H\alpha,broad}$. Our measured number density of BHAEs is generally consistent with Greene et al. (2024) and Matthee et al. (2023), considering the uncertainties induced by dust attenuation, different selection criteria, and the cosmic variance.

However, it is unclear whether it is reasonable to compare the bolometric LF of quasars with that of BHAEs. The conversion between Hα and bolometric luminosity in Equation (2) was calibrated based on the mid-infrared and optical properties of type 1 quasars at low redshifts. These high-redshift BHAEs may exhibit very different SEDs from those of typical quasars (e.g., Pérez-González et al. 2024). The estimated $L_{\rm bol}$ are subject to significant systematic uncertainties. The different bolometric correction recipes also introduce uncertainties (Runnoe et al. 2012; Duras et al. 2020). Multiwavelength observations and comprehensive analysis of

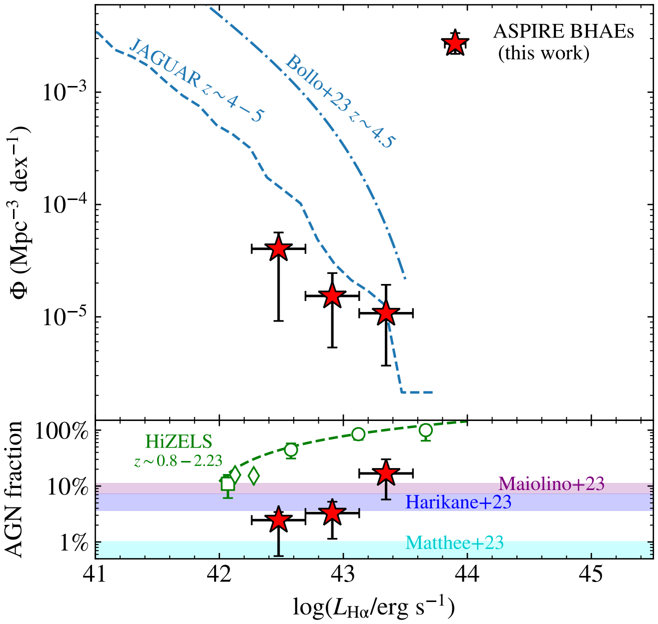

Figure 8. The Hα (broad + narrow) LF of the BHAEs (red stars). The Hα LF of Lyman break galaxies at $z\sim4.5$ is presented as the blue dashed–dotted line, and the prediction of JAGUAR mocks (Williams et al. 2018) for star-forming galaxies is presented as the blue dashed line. We show the fraction of BHAEs in each luminosity bin. The AGN fractions reported in Harikane et al. (2023), Matthee et al. (2023), and Maiolino et al. (2023) are labeled as cyan, blue, and purple shaded regions, respectively. For comparison, we show the AGN fraction from the HiZELs sample at $z\sim0.8$–2.23: the AGN fraction based on the BPT diagram (Stott et al. 2013) as the green square, the AGN fraction identified using Spitzer/IRAC colors (Sobral et al. 2016) as the green diamonds, and the AGN fraction by broad Hα components (Sobral et al. 2016) as the green circles.

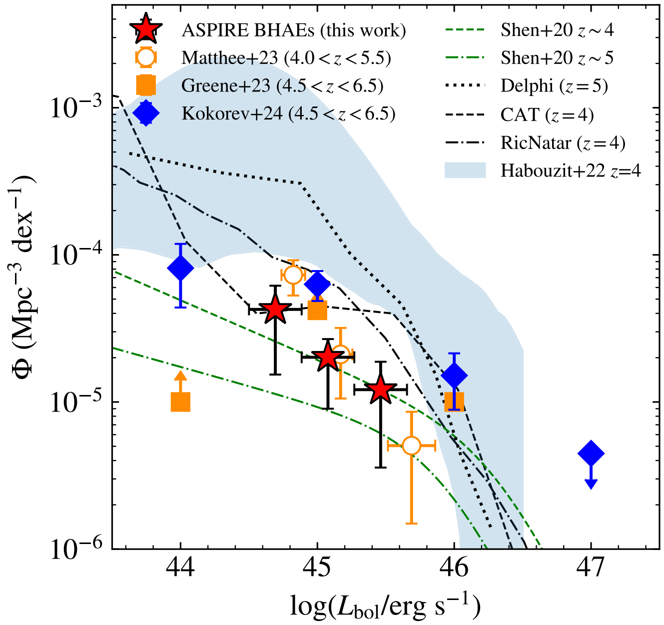

Figure 9. The bolometric LF of BHAEs (red stars). The bolometric luminosities of ASPIRE BHAEs are estimated based on the broad Hα luminosities. We also show the broad Hα-converted bolometric LF of $z\approx4.5$–6.5 AGNs in Greene et al. (2024) and the L_{5100}-converted bolometric LF in Kokorev et al. (2024) as the blue diamonds and orange squares, respectively, and convert the broad Hα LF of Matthee et al. (2023), which was not corrected for dust attenuation either, into the bolometric LF. The bolometric LFs of quasars at $z\sim4$ and $z\sim5$ are shown as the gray dashed and dashed–dotted lines, respectively (Shen et al. 2020). We also present the predicted AGN bolometric LFs of Delphi at $z=5$ (Dayal et al. 2019), CAT at $z=4$ (Trinca et al. 2022), Ricarte & Natarajan (2018) at $z=4$, and the range of AGN bolometric LFs at $z=4$ from different hydrodynamical cosmological simulations concluded in Habouzit et al. (2022).

Table 4
The Hα LF, BHAE Fraction, and Bolometric LF as Shown in Figures 8 and 9

$\log L_{\mathrm{H}\alpha}$	$\Delta\log L_{\mathrm{H}\alpha}$	N	Φ (10^{-5} Mpc^{-3} dex^{-1})	Frac (%)
42.478	0.433	6	$4.04^{+1.60}_{-3.12}$	$2.46^{+0.97}_{-1.90}$
42.911	0.433	6	$1.53^{+0.92}_{-1.00}$	$3.28^{+1.96}_{-2.14}$
43.345	0.433	4	$1.08^{+0.85}_{-0.71}$	$16.82^{+13.30}_{-11.07}$
$\log L_{\mathrm{bol}}$	$\Delta\log L_{\mathrm{bol}}$	N	Φ (10^{-5} Mpc^{-3} dex^{-1})	
44.692	0.385	5	$4.26^{+1.91}_{-2.72}$	
45.077	0.385	7	$2.01^{+0.66}_{-1.11}$	
45.462	0.385	4	$1.21^{+0.66}_{-0.85}$	

Note. The number densities and fractions are all lower limits since we do not correct for the completeness.

BHAE SEDs are essential to investigate their bolometric properties further.

4. Discussion

4.1. High Number Density of BHAEs

Figure 9 suggests a high AGN number density at the lower end of the bolometric luminosity, albeit with significant potential systematic uncertainties. We note that we do not apply any reddening correction in Figure 9. If we correct L_{bol} using a typical value of $A_V=2$, L_{bol} would increase by a factor of 2.3. Applying $A_V=4$ would increase L_{bol} by 6.9. Consequently, the bolometric LF would shift to the bright end by 0.4–0.8 dex, increasing the excess of BHAE number density over that of type 1 AGNs. As discussed in Greene et al. (2024), while the number density of AGNs is larger than what would be expected from the extrapolation of the quasar LF toward faint luminosities, a large number density of faint quasars is generally consistent with predictions from theoretical models, at least at $z<6.5$, while there may be some tension at the bright end for $z>6.5$. Indeed, the overprediction of the faint end of the LF appeared to be common, as shown, for instance, in the compilation of results from large-volume simulations of Habouzit et al. (2022). The updated AGN number densities are in much better agreement with the predicted large number of high-redshift faint AGNs. Most of these large-volume simulations, however, include simplistic predictions for BH formation and growth, since they cannot resolve the subparsec scales relevant for BH physics.

Semianalytical models tend to include more specific recipes for BH formation (e.g., Ricarte & Natarajan 2018; Dayal et al. 2019; Trinca et al. 2022). Many of these models are based on bimodal BH seed models: "light" seeds with mass $<10^3\,M_\odot$ remnants of the first stars, or "heavy" seeds with mass $>10^5\,M_\odot$ formed from the collapse of supermassive stars formed under very specific conditions (see Inayoshi et al. 2022; Volonteri et al. 2023, for reviews). They usually find that the number density of BH seeds decreases with the seed mass, but the ability to grow instead increases with the seed mass. Interestingly,

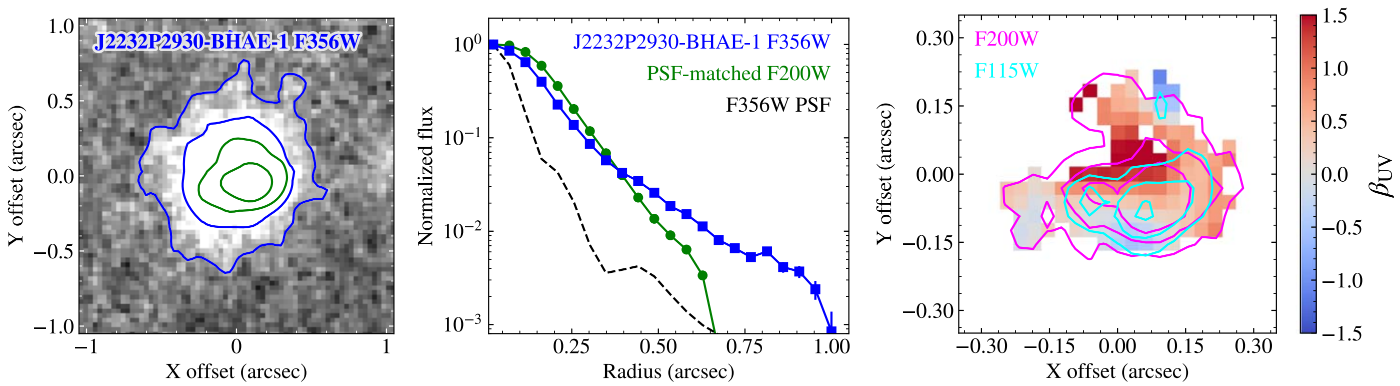

Figure 10. Left: JWST/NIRCam F356W image of J2232P2930-BHAE-1. The blue lines denote the 2σ and 7σ contours of the F356W image. The green lines are the 2σ and 7σ contours of the PSF-homogenized F200W image, matched to the F356W PSF. Middle: the surface brightness radial profile of J2232P290-BHAE-1. The blue squares show the F356W surface brightness profile of J2232P2930-BHAE-1, and the green circles show the profile of PSF-homogenized F200W. We show the radial profile of the F356W PSF as the black dashed line. Right: the UV slope map of J2232P2930-BHAE-1, produced using F115W and F200W images, PSF-matched to F200W. We smooth the map using a 1-pixel Gaussian kernel. The magenta and cyan lines denote the 2σ, 5σ, and 10σ contours of the F115W and F200W images, respectively.

recent simulations and theoretical models of BH seed formation suggest a less extremely bimodal situation (e.g., Regan et al. 2020; Schleicher et al. 2022), with numerous seeds at mass $\sim 10^3\ M_\odot$, more consistent with a widespread population of relatively bright AGNs presented in this paper.

Finally, as discussed in Section 3.5, the observed high-redshift BHAE population is not yet fully characterized. The bolometric luminosity of BHAEs might not be well described by Equation (2). A valid comparison of BHAE number density between simulations and observations relies on thoroughly understanding BHAEs' nature, bolometric properties, selection function, and completeness through future observations.

4.2. Evidence of Clustering of BHAEs

In this section we present early evidence of strong clustering of BHAEs.

4.2.1. A Pair of BHAEs

J1526M2050-BHAE-2 and J1526M2050-BHAE-3, both at $z = 4.87$, are $1\rlap{.}'36$ apart from each other, corresponding to a projected separation of 519 pkpc. The velocity offset between the two is $\approx 222\ \mathrm{km\ s^{-1}}$. There might be physical connections between these two BHAEs, which could reside in the same overdensity or large-scale structure. A systematic search for galaxies at a similar redshift is needed for further detailed studies.

4.2.2. J2232P2930-BHAE-1: An Extended Hα Emitter with Close Neighbors

Among the 15 ASPIRE BHAEs presented in this paper, J2232P2930-BHAE-1 at $z = 4.135$ has the brightest F356W magnitude ($m_{\mathrm{F356W}} = 23.39$) and a very high H$\alpha$ luminosity ($L_{\mathrm{H\alpha,tot}} = 2 \times 10^{43}\ \mathrm{erg\ s^{-1}}$). Its F356W morphology is more extended than that in the F200W band, indicative of diffuse extended Hα emission. We present its F356W image, its PSF-homogenized F200W contour, and the corresponding radial profiles in the left and middle panels of Figure 10. Its F115W and F200W images reveal four marginally resolved components as shown in the right panel of Figure 10. It also shows significant spatial variation in β_{UV}. The upper component ($(x, y) = (0'', 0\rlap{.}''15)$) has a red UV slope ($\beta_{\mathrm{UV}} \gtrsim 1$), and the left component is comparatively blue ($\beta_{\mathrm{UV}} \lesssim -0.5$). It is not clear whether there is β_{UV} variation in the two central F200W contour peaks, limited by the spatial resolution of F200W. The variation of β_{UV} might be caused by the inhomogeneous distribution of dust content. As a composite system with multiple components, the broad-line profile of J2232P2930-BHAE-1 could be a result of blended Hα emission from individual substructures, and not necessarily corresponding to an AGN BLR. Future observations with JWST/NIRSpec IFU are required to investigate its internal structure.

Moreover, J2232P2930-BHAE-1 has three close companion galaxies at the same redshift. As shown in Figure 11, the three companion galaxies, named Companion-1, Companion-2, and Companion-3, are $2\rlap{.}''1$, $1\rlap{.}''6$, and $3\rlap{.}''85$ away from J2232P2930-BHAE-1, respectively, corresponding to 14.5, 10.8, and 26.4 pkpc at $z = 4.13$. Companion-1, Companion-2, and Companion-3 have Hα luminosities of $(1.7 \pm 0.7) \times 10^{42}\ \mathrm{erg\ s^{-1}}$, $(1.9 \pm 0.2) \times 10^{42}\ \mathrm{erg\ s^{-1}}$, and $(5.2 \pm 0.5) \times 10^{41}\ \mathrm{erg\ s^{-1}}$, respectively. This implies that J2232P2930-BHAE-1 may reside in an overdense region. There is a tentative detection of diffuse Hα emission between Companion-2 and J2232P2930-BHAE-1, as shown in both the RGB image (left panel of Figure 11) and the 2D grism spectrum (middle panel of Figure 11), indicating possible interaction between the two sources. Detailed studies on the environment of J2232P2930-BHAE-1 will be performed in future works with a systematic search for Hα emitters at the same redshift.

4.3. Blueshifted Hα Absorption

J0923P0402-BHAE-1, J1526M2050-BHAE-1, and J1526M2050-BHAE-3 present blueshifted absorption features on top of their Hα emission lines. The velocity offsets between the absorption and the Hα emission peak for J0923P0402-BHAE-1, J1526M2050-BHAE-1, and J1526M2050-BHAE-3 are 586, 357, and 266 $\mathrm{km\ s^{-1}}$, respectively.

If these features are Hα absorption of high column density gas, the fraction is high (19% in ASPIRE BHAEs, 10% in the sample of Matthee et al. 2023, 15% in the sample of Kocevski et al. 2024) compared to low-redshift type 1 AGNs (<0.1%; e.g., Aoki et al. 2006; Zhang et al. 2018), as shown in Figure 12. The prevalence of Hα absorption, if confirmed, suggests that these high-redshift BHAEs could differ

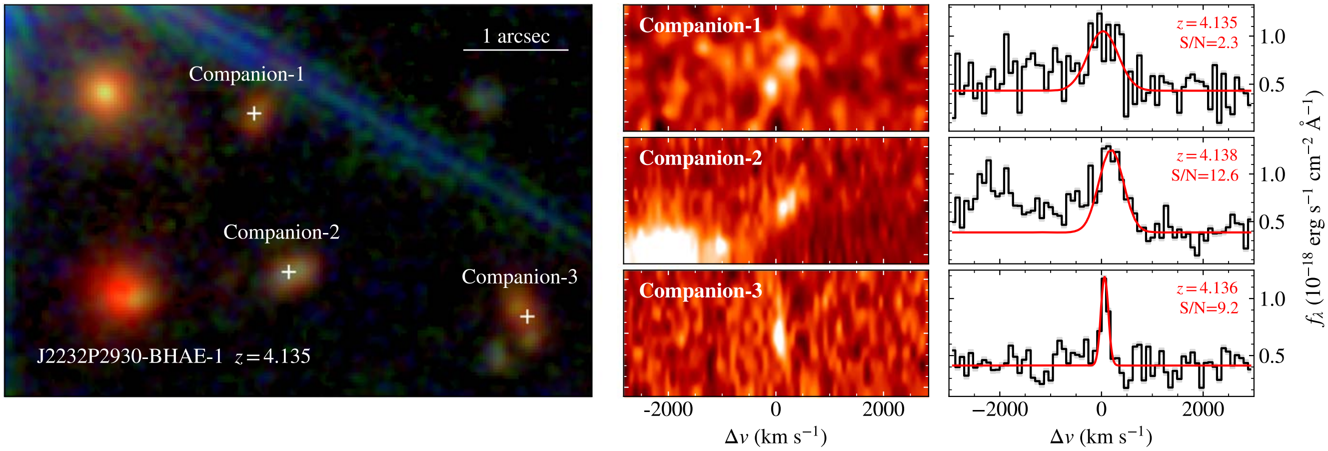

Figure 11. J2232P2930-BHAE-1 and its three neighboring galaxies. The left panel shows the RGB image composed of F115W, F200W, and F356W. We label the three companion galaxies using white plus signs. In the middle panel we present the 2D WFSS spectra of the three galaxies, and the extracted 1D spectra are shown in the right panel. The 2D and 1D spectra are both displayed in the velocity frame relative to J2232P2930-BHAE-1. We can see tentative diffuse Hα gas between Companion-2 and J2232P2930-BHAE-1 in the RGB image and the 2D grism, suggesting possible interaction between the two sources.

significantly from low-redshift type 1 AGNs. High-redshift BHAEs may contain abundant outflowing dense gas, which could be related to either BH activity or strong galactic feedback in the host galaxies.

4.4. Comparison with Literature LRDs and Selection Effect

We compare photometrically and broad-line-selected samples in the literature in Figure 13. The broad-line-selected samples (e.g., ASPIRE; Matthee et al. 2023; Harikane et al. 2023), which impose no constraints on the SED shapes, contain BHAEs with $\beta_{\rm opt} \lesssim 0$, as illustrated in the left panel of Figure 13. On the other hand, the samples photometrically selected based on V-shaped SEDs (Greene et al. 2024 and Kocevski et al. 2024) do not include such objects. Meanwhile, the broad-line-selected BHAEs lack UV-luminous but red objects (with $M_{\rm UV} \lesssim -19.5$ and $\beta_{\rm opt} > 0$).

The photometric selection requiring V-shaped SEDs is biased toward sources with reddened rest-frame optical spectra and against those with relatively blue optical continua ($\beta_{\rm opt} < 0$). The flux-limited broad-line selection fails to detect objects with weak broad Hα flux, as their Hα broad wings could be overwhelmed by background noise. As shown in the middle panel of Figure 13, the UV-luminous and red sources in Greene et al. (2024) exhibit broad Hα luminosity lower than those of most JWST/WFSS-selected BHAEs. Their broad Hα components may not be reliably identified with the shallow grism data. We note that among the NIRSpec-selected sample from Harikane et al. (2023), the two sources with reddened rest-frame optical continua also have the faintest $M_{\rm UV}$ ($M_{\rm UV} > -18$). Since their broad-line selection relies on archive data, the prior source selection for the NIRSpec MSA is crucial but can be intricate.

The distribution of grism-selected BHAEs on the $\beta_{\rm opt}$–$M_{\rm UV}$ and $M_{\rm UV}$–EW$_{\rm H\alpha,broad}$ planes (the left and right panels of Figure 13) is attributed to the flux-limited selection effect. The absence of UV-faint and optical-blue objects ($M_{\rm UV} \gtrsim -18$ and $\beta_{\rm opt} < 0$) can be attributed to their weak broad Hα wings falling below the detection limit, as they might have lower-mass BHs and host galaxies following the coevolution of the BH−galaxy. Although the UV-luminous and optically red BHAEs ($M_{\rm UV} > -19$ and $\beta_{\rm opt} > 0$) missing from the grism-selected sample all have low $L_{\rm H\alpha,broad}$, similar objects with high $L_{\rm H\alpha,broad}$ might exist but are rare owing to the rapid decline toward the bright end of the LFs. On the other hand, it remains unclear whether BHAEs with $\beta_{\rm opt} > 0$ and $\beta_{\rm opt} < 0$ belong to the same population. A plausible interpretation is that $\beta_{\rm opt} < 0$ BHAEs may closely resemble type 1 quasars. It is also possible that BHAEs with $\beta_{\rm opt} < 0$ are counterparts of those with $\beta_{\rm opt} > 0$, but with less obscured AGN components. In this case, if the UV emission originates from the host galaxies, the stellar light from UV-luminous star-forming galaxies may contribute significantly to the rest-frame optical spectra, potentially leading to a bluer $\beta_{\rm opt}$.

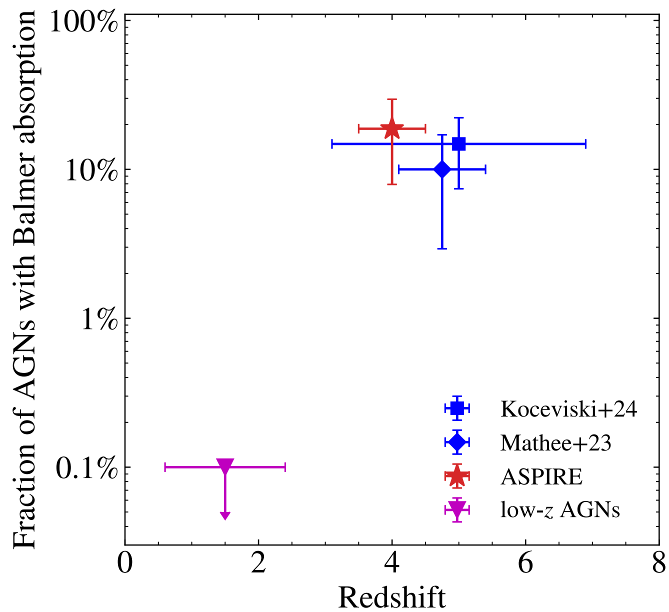

Figure 12. The fraction of AGNs with Balmer absorption across the cosmic time. The error bars in the redshift axis indicate the redshift range of the AGN sample, while the uncertainties in the fraction on the y-axis are calculated assuming a Poisson distribution.

We notice that the two optically red BHAEs identified in Harikane et al. (2023) are both compact and point-source-like, in contrast to the other objects they selected, which either are extended or have bright companions. The depth of ASPIRE images does not allow us to resolve the morphology of

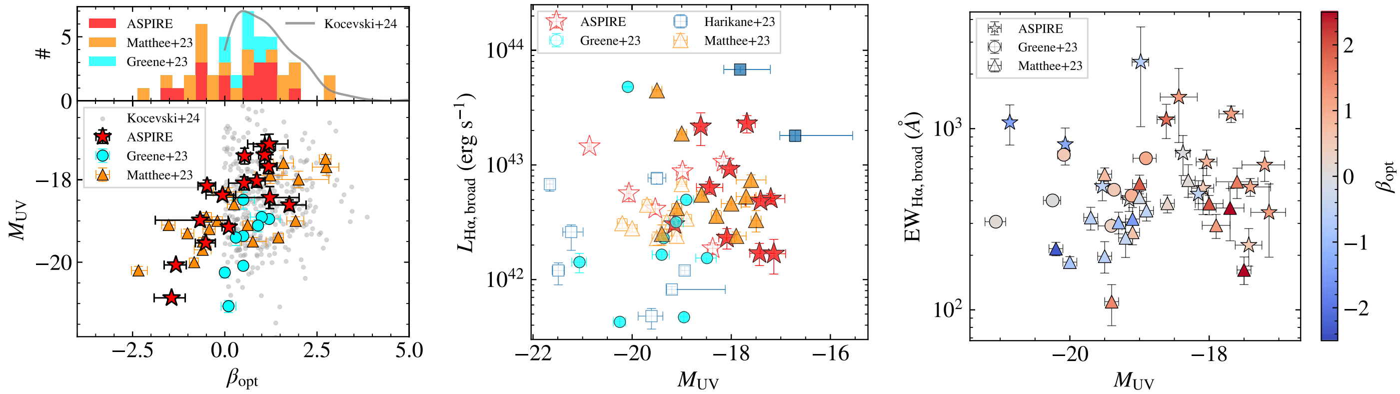

Figure 13. Left panel: the β_{opt} vs. M_{UV} distribution of JWST broad-line-selected and photometrically selected LRDs. The broad-line-selected samples include the ASPIRE BHAEs (red) and the BHAEs in Matthee et al. (2023; orange). The photometrically selected samples include spectroscopically confirmed BHAEs in Greene et al. (2024; cyan) and LRDs in Kocevski et al. (2024; gray). We show the density distribution of β_{opt} for the Kocevski et al. (2024) sample. Middle panel: the broad Hα luminosity vs. M_{UV}. The filled markers denote the BHAEs with reddened optical continua ($\beta_{opt} > 0$), while white ones have $\beta_{opt} < 0$. Right panel: the rest-frame equivalent width of the broad Hα vs. M_{UV}, color-coded by β_{opt}.

individual BHAEs. Instead, we examine the BHAEs in Matthee et al. (2023). Among the nine BHAEs with $\beta_{opt} < 0$ in Matthee et al. (2023), seven have extended F200W (or F182M + F210M) morphologies, and only two are compact and point-source-like. Among the 11 $\beta_{opt} > 0$ BHAEs, four show significant extended F200W morphologies, and the remaining seven are compact. The "compactness rate" is 63% for $\beta_{opt} > 0$ BHAEs compared to 22% for $\beta_{opt} < 0$ BHAEs. This can also be due to a selection effect. As discussed above, the grism-selected BHAE sample misses UV-luminous but optically red objects, and as shown in the left panel of Figure 13, the grism-selected $\beta_{opt} > 0$ BHAEs are all UV faint. Their UV faintness makes it challenging to resolve the extended components in short-wavelength images. To conclusively determine whether there is any potential correlation between optical redness and morphologies, a larger and unbiased sample is essential.

In summary, different selection criteria introduce various biases that must be carefully considered to understand the nature of this newly discovered BHAE population. A systematic classification is essential for understanding their properties. To explore a broader range of samples in the future, a more inclusive selection criterion that considers both AGN and galaxy contributions in the rest-frame optical band is necessary.

5. Summary

We report the discovery of 16 BHAEs at $z = 4$–5 selected from the JWST ASPIRE program. These BHAEs are primarily selected as a result of their compactness and redness. Their broad Hα emission lines are identified utilizing the JWST/NIRCam WFSS of F356W. Our main results are summarized below.

1. The ASPIRE BHAEs exhibit broad Hα emission components with FWHM (FWHM$_{broad}$) ranging from 1000 to 3000 km s^{-1} and luminosity ($L_{H\alpha,broad}$) ranging from 10^{42} to $\gtrsim 10^{43}$ erg s^{-1}. The fraction of Hα flux in the broad components ($L_{H\alpha,broad}/L_{H\alpha,total}$) spans a wide range from ∼0.4 up to 1, with a median value of 0.7. These BHAEs are distributed similarly in the FWHM$_{broad}$ − $L_{H\alpha,broad}$ diagram compared to low-redshift ($z < 0.6$) SDSS quasars. On the other hand, BHAEs have lower $L_{H\alpha,broad}/L_{H\alpha,total}$ than most of the SDSS quasars, suggesting larger contributions from the host galaxies or NLRs to the total Hα luminosity.
2. The BH masses (M_{BH}) of ASPIRE BHAEs range from $\sim 10^7$ to $\sim 10^8$ $M_\odot$, comparable to those of BHs in low-redshift SDSS quasars. The Hα converted bolometric luminosity (L_{bol}) suggests that these BHAEs are accreting at Eddington ratios of 0.07–0.47, with a median value of 0.17.
3. In general, the ASPIRE BHAEs have UV continuum slopes (β_{UV}) bluer than the optical continuum slopes (β_{opt}). In contrast to Matthee et al. (2023), we do not see significant correlations between β_{opt} and $L_{H\alpha,broad}/L_{H\alpha,total}$ or M_{BH}.
4. The stacked images of ASPIRE BHAE show extended components in F200W. The F200W stack extends to $\sim 0\farcs4$, corresponding to 2.6 pkpc at $z \sim 4.5$. The extended morphologies in F115W and F356W are tentative and limited by the shallow depth of observations. The extended structure suggests the presence of host galaxies.
5. The Hα LF of ASPIRE BHAEs suggests that the AGN fraction increases toward higher Hα luminosities, consistent with low-redshift Hα emitters. The BHAE fraction spans from 2% at total Hα luminosity of $\log(L_{H\alpha}/\mathrm{erg\ s^{-1}}) \approx 42.5$ to 17% at $\log(L_{H\alpha}/\mathrm{erg\ s^{-1}}) \approx 43.3$.
6. We find a pair of BHAEs at the same redshift ($z \approx 4.87$) with a separation of 519 pkpc. Another isolated BHAE, J2232P2930-BHAE-1, as a composite system with bright extended Hα emission and significant β_{UV} variation, resides in an overdense region with three close companion galaxies. These, for the first time, provide tentative evidence for the strong clustering of BHAEs.
7. We find three BHAEs with blueshifted Hα absorption, potentially indicating the presence of outflowing dense gas. The prevalence of Hα absorption (19% in ASPIRE BHAEs) might be a unique feature of this high-redshift AGN population.
8. We compare the broad-line-selected and photometrically selected BHAE samples from the literature. The photometrically selected sample, based on the V-shaped SED, does not contain optically blue ($\beta_{opt} < 0$) objects, while the flux-limited grism-selected sample lacks UV-luminous but optically red ($M_{UV} \lesssim -19.5$ and $\beta_{opt} > 0$)

objects. The optically red BHAEs tend to be more compact in rest-frame UV bands. However, these differences can be explained by the selection effect. A more inclusive selection method is needed to study a broader range of BHAEs.

The ASPIRE BHAE sample with spectroscopically identified broad Hα emission provides a good database for further studies on low-luminosity AGNs in the early Universe. To further investigate the nature of high-redshift low-luminosity AGNs and their roles on the evolutionary tracks of early BH assembly, future follow-ups in both the rest-frame UV and infrared wavelengths are required. Deep spectroscopic and IFU observations covering the UV continua and emission lines can provide constraints on the origin of the extended blue components. Observations in the infrared band with JWST/MIRI are crucial to determine the full SED shapes and to understand the roles of AGNs and starbursts in these broad-line-selected samples.

Acknowledgments

X.L. and Z.C. are supported by the National Key R&D Program of China (grant No. 2023YFA1605600), the National Science Foundation of China (grant No. 12073014), the science research grants from the China Manned Space Project with No. CMS-CSST-2021-A05, and the Tsinghua University Initiative Scientific Research Program (No. 20223080023). F.W. and X.F. acknowledge support from NSF grant AST-2308258. F.S. acknowledges JWST/NIRCam contract to the University of Arizona NAS5-02015. J.B.C. acknowledges funding from the JWST Arizona/Steward Postdoc in Early Galaxies and Reionization (JASPER) Scholar contract at the University of Arizona. A.L. acknowledges support by the PRIN MUR "2022935STW." M.T. acknowledges support from the NWO grant 016.VIDI.189.162 ("ODIN"). J.-T.S. is supported by the Deutsche Forschungsgemeinschaft (DFG, German Research Foundation) - Project No. 518006966.

This work is based on observations made with the NASA/ESA/CSA James Webb Space Telescope. The data were obtained from the Mikulski Archive for Space Telescopes at the Space Telescope Science Institute, which is operated by the Association of Universities for Research in Astronomy, Inc., under NASA contract NAS 5-03127 for JWST. These observations are associated with program No. 2078. The specific observations analyzed can be accessed via doi:10.17909/vt74-kd84. Support for this program was given through a grant from the Space Telescope Science Institute, which is operated by the Association of Universities for Research in Astronomy, Inc., under NASA contract NAS 5-03127.

Facility: JWST.

Software: JWST calibration pipeline (v1.10.2 Bushouse et al. 2023) SciPy (Virtanen et al. 2020) SExtractor++ (Bertin et al. 2020).

ORCID iDs

Xiaojing Lin https://orcid.org/0000-0001-6052-4234
Feige Wang https://orcid.org/0000-0002-7633-431X
Xiaohui Fan https://orcid.org/0000-0003-3310-0131
Zheng Cai https://orcid.org/0000-0001-8467-6478
Jaclyn B. Champagne https://orcid.org/0000-0002-6184-9097
Fengwu Sun https://orcid.org/0000-0002-4622-6617
Marta Volonteri https://orcid.org/0000-0002-3216-1322
Jinyi Yang https://orcid.org/0000-0001-5287-4242
Joseph F. Hennawi https://orcid.org/0000-0002-7054-4332
Eduardo Bañados https://orcid.org/0000-0002-2931-7824
Aaron Barth https://orcid.org/0000-0002-3026-0562
Anna-Christina Eilers https://orcid.org/0000-0003-2895-6218
Emanuele Paolo Farina https://orcid.org/0000-0002-6822-2254
Weizhe Liu https://orcid.org/0000-0003-3762-7344
Xiangyu Jin https://orcid.org/0000-0002-5768-738X
Hyunsung D. Jun https://orcid.org/0000-0003-1470-5901
Alessandro Lupi https://orcid.org/0000-0001-6106-7821
Koki Kakiichi https://orcid.org/0000-0001-6874-1321
Chiara Mazzucchelli https://orcid.org/0000-0002-5941-5214
Masafusa Onoue https://orcid.org/0000-0003-2984-6803
Zhiwei Pan https://orcid.org/0000-0003-0230-6436
Sofía Rojas-Ruiz https://orcid.org/0000-0003-2349-9310
Jan-Torge Schindler https://orcid.org/0000-0002-4544-8242
Benny Trakhtenbrot https://orcid.org/0000-0002-3683-7297
Yue Shen https://orcid.org/0000-0003-1659-7035
Maxime Trebitsch https://orcid.org/0000-0002-6849-5375
Ming-Yang Zhuang https://orcid.org/0000-0001-5105-2837
Romain A. Meyer https://orcid.org/0000-0001-5492-4522
Zihao Li https://orcid.org/0000-0001-5951-459X
Mingyu Li https://orcid.org/0000-0001-6251-649X
Maria Pudoka https://orcid.org/0000-0003-4924-5941
Yunjing Wu https://orcid.org/0000-0003-0111-8249
Haowen Zhang https://orcid.org/0000-0002-4321-3538

References

Aoki, K., Iwata, I., Ohta, K., et al. 2006, ApJ, 651, 84
Bañados, E., Venemans, B. P., Mazzucchelli, C., et al. 2018, Natur, 553, 473
Barro, G., Perez-Gonzalez, P. G., Kocevski, D. D., et al. 2023, ApJ, 963, 128
Bertin, E., Schefer, M., Apostolakos, N., et al. 2020, in ASP Conf. Ser. 527, Astronomical Data Analysis Software and Systems XXIX, ed. R. Pizzo et al. (San Francisco, CA: ASP), 461
Bollo, V., González, V., Stefanon, M., et al. 2023, ApJ, 946, 117
Bushouse, H., Eisenhamer, J., Dencheva, N., et al. 2023, JWST Calibration Pipeline v1.10.2, Zenodo, doi:10.5281/zenodo.7829329
Dayal, P., Rossi, E. M., Shiralilou, B., et al. 2019, MNRAS, 486, 2336
Ding, X., Onoue, M., Silverman, J. D., et al. 2023, Natur, 621, 51
Duras, F., Bongiorno, A., Ricci, F., et al. 2020, A&A, 636, A73
Fan, X., Bañados, E., & Simcoe, R. A. 2023, ARA&A, 61, 373
Farina, E. P., Schindler, J.-T., Walter, F., et al. 2022, ApJ, 941, 106
Furtak, L. J., Labbé, I., Zitrin, A., et al. 2024, Natur, 628, 57
Gaia Collaboration, Brown, A. G. A., Vallenari, A., et al. 2018, A&A, 616, A1
Gaia Collaboration, Prusti, T., de Bruijne, J. H. J., et al. 2016, A&A, 595, A1
Gehrels, N. 1986, ApJ, 303, 336
Greene, J. E., & Ho, L. C. 2005, ApJ, 630, 122
Greene, J. E., Labbe, I., Goulding, A. D., et al. 2024, ApJ, 964, 39
Greene, T. P., Chu, L., Egami, E., et al. 2016, Proc. SPIE, 9904, 99040E
Habouzit, M., Somerville, R. S., Li, Y., et al. 2022, MNRAS, 509, 3015
Hainline, K. N., Helton, J. M., Johnson, B. D., et al. 2024, ApJ, 964, 66
Harikane, Y., Zhang, Y., Nakajima, K., et al. 2023, ApJ, 959, 39
Inayoshi, K., Onoue, M., Sugahara, Y., Inoue, A. K., & Ho, L. C. 2022, ApJL, 931, L25
Killi, M., Watson, D., Brammer, G., et al. 2023, arXiv:2312.03065
Kocevski, D. D., Finkelstein, S. L., Barro, G., et al. 2024, arXiv:2404.03576
Kocevski, D. D., Onoue, M., Inayoshi, K., et al. 2023, ApJL, 954, L4
Kokorev, V., Caputi, K. I., Greene, J. E., et al. 2024, ApJ, 968, 38
Kokorev, V., Fujimoto, S., Labbe, I., et al. 2023, ApJL, 957, L7
Kron, R. G. 1980, ApJS, 43, 305
Labbe, I., Greene, J. E., Bezanson, R., et al. 2023, arXiv:2306.07320
Li, J., Silverman, J. D., Shen, Y., et al. 2024, arXiv:2403.00074
Maiolino, R., Scholtz, J., Curtis-Lake, E., et al. 2023, arXiv:2308.01230
Matthee, J., Naidu, R. P., Brammer, G., et al. 2023, ApJ, 963, 129
Mazzucchelli, C., Bischetti, M., D'Odorico, V., et al. 2023, A&A, 676, A71
Onoue, M., Inayoshi, K., Ding, X., et al. 2023, ApJL, 942, L17
Onoue, M., Kashikawa, N., Matsuoka, Y., et al. 2019, ApJ, 880, 77
Pacucci, F., Nguyen, B., Carniani, S., Maiolino, R., & Fan, X. 2023, ApJL, 957, L3
Peng, C. Y., Ho, L. C., Impey, C. D., & Rix, H.-W. 2002, AJ, 124, 266

Pérez-González, P. G., Barro, G., Rieke, G. H., et al. 2024, ApJ, 968, 4
Prochaska, J., Hennawi, J., Westfall, K., et al. 2020, JOSS, 5, 2308
Regan, J. A., Wise, J. H., Woods, T. E., et al. 2020, OJAp, 3, 15
Reines, A. E., Greene, J. E., & Geha, M. 2013, ApJ, 775, 116
Reines, A. E., & Volonteri, M. 2015, ApJ, 813, 82
Ricarte, A., & Natarajan, P. 2018, MNRAS, 481, 3278
Richards, G. T., Lacy, M., Storrie-Lombardi, L. J., et al. 2006, ApJS, 166, 470
Runnoe, J. C., Brotherton, M. S., & Shang, Z. 2012, MNRAS, 422, 478
Schleicher, D. R. G., Reinoso, B., Latif, M., et al. 2022, MNRAS, 512, 6192
Schmidt, M. 1968, ApJ, 151, 393
Scholtz, J., Maiolino, R., D'Eugenio, F., et al. 2023, arXiv:2311.18731
Shen, X., Hopkins, P. F., Faucher-Giguère, C.-A., et al. 2020, MNRAS, 495, 3252
Shen, Y., Richards, G. T., Strauss, M. A., et al. 2011, ApJS, 194, 45
Shen, Y., Wu, J., Jiang, L., et al. 2019, ApJ, 873, 35
Sobral, D., Kohn, S. A., Best, P. N., et al. 2016, MNRAS, 457, 1739
Stott, J. P., Sobral, D., Bower, R., et al. 2013, MNRAS, 436, 1130
Sun, F., Egami, E., Pirzkal, N., et al. 2023, ApJ, 953, 53
Trakhtenbrot, B., Netzer, H., Lira, P., & Shemmer, O. 2011, ApJ, 730, 7
Trinca, A., Schneider, R., Valiante, R., et al. 2022, MNRAS, 511, 616
Übler, H., Maiolino, R., Curtis-Lake, E., et al. 2023, A&A, 677, A145
Virtanen, P., Gommers, R., Oliphant, T. E., et al. 2020, NatMe, 17, 261
Volonteri, M. 2010, A&ARv, 18, 279
Volonteri, M., Habouzit, M., & Colpi, M. 2023, MNRAS, 521, 241
Wang, F., Yang, J., Fan, X., et al. 2021, ApJL, 907, L1
Wang, F., Yang, J., Hennawi, J. F., et al. 2023, ApJL, 951, L4
Williams, C. C., Alberts, S., Ji, Z., et al. 2024, ApJ, 968, 34
Williams, C. C., Curtis-Lake, E., Hainline, K. N., et al. 2018, ApJS, 236, 33
Wu, Q., & Shen, Y. 2022, ApJS, 263, 42
Yang, J., Fan, X., Gupta, A., et al. 2023, ApJS, 269, 27
Yang, J., Wang, F., Fan, X., et al. 2021, ApJ, 923, 262
Zhang, S., Zhou, H., Shi, X., et al. 2018, AJ, 156, 4